Corrosion of Zirconium Alloys Used for Nuclear Fuel Cladding

Arthur T. Motta,[1] Adrien Couet,[1] and Robert J. Comstock[2]

[1]Department of Mechanical and Nuclear Engineering, Pennsylvania State University, University Park, Pennsylvania 16802; email: atm2@psu.edu

[2]Westinghouse Electric Company LLC, Pittsburgh, Pennsylvania 15235

Annu. Rev. Mater. Res. 2015. 45:311–43

First published online as a Review in Advance on April 22, 2015

The *Annual Review of Materials Research* is online at matsci.annualreviews.org

This article's doi: 10.1146/annurev-matsci-070214-020951

Keywords

waterside corrosion, hydrogen pickup, zirconium alloys

Abstract

During operation, nuclear fuel rods are immersed in the primary water, causing waterside corrosion and consequent hydrogen ingress. In this review, the mechanisms of corrosion and hydrogen pickup and the role of alloy selection in minimizing both phenomena are considered on the basis of two principal characteristics: the pretransition kinetics and the loss of oxide protectiveness at transition. In zirconium alloys, very small changes in composition or microstructure can cause significant corrosion differences so that corrosion performance is strongly alloy dependent. The alloys show different, but reproducible, subparabolic pretransition kinetics and transition thicknesses. A mechanism for oxide growth and breakup based on a detailed study of the oxide structure can explain these results. Through the use of the recently developed coupled current charge compensation model of corrosion kinetics and hydrogen pickup, the subparabolic kinetics and the hydrogen fraction can be rationalized: Hydrogen pickup increases when electron transport decreases, requiring hydrogen ingress to close the reaction.

1. INTRODUCTION

The majority of commercial nuclear reactors in the world today are light water reactors: either pressurized water reactors (PWRs) or boiling water reactors (BWRs). The nuclear fuel used in these reactors is in the form of fuel rods, which consist of long tubes (approximately 4 m long, with approximately 1-cm diameter and 0.6-mm wall thickness) made out of zirconium alloys and which contain uranium dioxide pellets. These tubes, termed the nuclear fuel cladding, constitute the first barrier against the release of fission products into the primary circuit. Because of this important function, it is crucial to nuclear safety to ensure cladding integrity during service.

Various degradation processes—including grid-to-rod fretting, debris-induced failures, crud-induced localized corrosion, waterside corrosion, and hydriding—may challenge the integrity of the cladding tube; these processes are summarized in Reference 1. In this review, we focus on the last two processes of waterside corrosion and hydrogen pickup and on the role of alloy selection in minimizing both. During operation, the nuclear fuel rods are immersed in the primary circuit water, which circulates through the core to extract the heat to produce nuclear electricity. Although the high outlet temperatures (to maximize thermal efficiency, the outlet temperatures in PWRs and BWRs are approximately 330°C and 288°C, respectively) favor the cladding-water corrosion reaction and the associated hydrogen pickup, careful alloy design can minimize the rates of these phenomena.

The history of the development of zirconium alloys for nuclear power gives some insight into the suite of alloys that we currently have. The zirconium-based alloys used for nuclear fuel cladding were first developed in the US Nuclear Navy program in the 1950s (2, 3). It was recognized early on that, in contrast to other alloy systems, the corrosion performance of zirconium alloys worsened as the alloy became more pure, with the purest metal exhibiting breakaway corrosion (4). It was found that almost any alloying addition initially increased corrosion resistance (5). A further unusual feature of the zirconium alloy system is that a very small proportion of alloying element additions (typically less than 0.5%) is sufficient to effect significant changes in corrosion behavior. The discovery of this sensitivity of zirconium alloy corrosion to small alloying additions caused a systematic search for alloying elements that improved both corrosion resistance and mechanical properties and that were not ruled out by large neutron cross sections.

Two main alloy systems were considered: In the United States, a zirconium-tin-based system gave rise to the Zircaloy family, whereas other countries (such as Canada and Russia) used a zirconium-niobium system. The zirconium-tin system first yielded Zircaloy-1 (Zr–1.5% Sn), which performed reasonably well but which was much improved upon by an accidental contamination of a melt by stainless steel, yielding an approximate composition of Zr–1.5% Sn, 0.14% Fe, 0.10% Cr, 0.06% Ni. This alloy was dubbed Zircaloy-2 (3). After the failure of Zircaloy-3 from metallurgical processing issues, concerns with the high hydrogen pickup fraction exhibited by Zircaloy-2 led to the development of Zircaloy-4, in which a higher Fe content substituted for Ni, which was believed to be the cause of high hydrogen ingress (2). These alloys were used from the 1950s to the 1990s; Zircaloy-4 was used in PWRs and Zircaloy-2 in BWRs. More recently, modern alloys such as ZIRLO® (6, 7) and M5™ (8)[1] have replaced Zircaloy-4 as the alloy of choice in PWRs, although Zircaloy-2 is still used in BWRs, albeit with a zirconium inner liner to protect against pellet cladding mechanical interaction–induced stress-corrosion cracking. This type of fuel cladding containing a coextruded inner liner of pure zirconium was termed barrier or duplex cladding (9).

[1]ZIRLO®, Optimized ZIRLO™, and AXIOM™ are registered trademarks or trademarks of Westinghouse Electric Company LLC in the United States and may be registered in other countries throughout the world. All rights reserved. Unauthorized use is strictly prohibited. M5™ is a trademark of AREVA NP registered in the United States and in other countries.

Throughout these decades, even in the face of increasingly severe fuel duty (higher temperatures, higher fuel burnup and residence time, more aggressive chemistry, presence of boiling in PWRs), the corrosion performance of zirconium alloys has steadily improved. This improvement was achieved through systematic modifications in alloy composition, fabrication procedures, and thermomechanical treatment. However, fundamental understanding of the specific role of alloying elements in the corrosion process is still lacking.

Over the years, there have been many reviews focusing on zirconium alloy corrosion (10–15). In particular, we highlight Cox's (11) 2005 review, in which he posed four questions. (*a*) What are the mobile species during corrosion? (*b*) Why does pretransition follow subparabolic kinetics? (*c*) What processes lead to oxide breakdown? (*d*) What role, if any, does hydrogen play in the process? In this review, we expand upon these questions and discuss recent experimental results and efforts to develop fundamental understanding of the role of oxide microstructure and alloying element composition in reducing the corrosion and hydrogen pickup in service. The in-reactor performance of zirconium alloys is first reviewed, followed by a review of the basics of the corrosion reaction and a discussion of oxide microstructure development, hydrogen pickup, and a unified model of corrosion and hydrogen pickup that addresses these issues.

2. IN-REACTOR PERFORMANCE

Significant effort in the industry has led to the development of improved alloys to meet the demands of higher fuel duty, increased cycle length (from 12 to 24 months), higher coolant temperature for increased efficiency, and more aggressive water chemistries. Due to the higher operating temperature of PWRs compared with that of BWRs, most of the effort has focused on alloys to improve or replace Zircaloy-4. Most efforts in the 1980s focused on optimizing chemistry and thermal processing of Zircaloy-4, but only modest improvements were realized. The most notable change was the reduction in Sn from 1.5% to 1.3% while remaining within the specification range of 1.2% to 1.7%.

Table 1 identifies some of the alloys that have been irradiated to high burnups in PWRs, with the goal of identifying alloys with improved performance. Whereas Zircaloy-4 was used in western PWR plants, the Russian alloy E110 was used in VVERs (Russian reactors, similar to PWRs). Unlike the Sn-based Zircaloys, E110 was a binary Zr–1% Nb alloy. A second Russian alloy for VVER application was E635, which contained both Sn and Nb. The first departure from Zircaloy-4 in western plants was the introduction of lead assemblies containing ZIRLO clad fuel in 1987 (6, 16). The motivations for the development of ZIRLO were the uncertainty in the extent of irradiation-enhanced corrosion and the projected increase in fuel duty.

Because an important limit in the licensing of fuel is burnup, plotting oxide thickness as a function of burnup has been common practice. However, burnup does not take into account the large variation in operating conditions from plant to plant and along the length of a fuel rod. **Figure 1** shows typical oxide thicknesses along a PWR fuel rod. The limiting oxide thickness occurs in the upper spans of the fuel assembly, where the coolant temperature is highest. A modified fuel duty index (MFDI) was introduced to take into account the impact of temperature and boiling (17). The relative improvement in corrosion performance is more clearly seen in **Figure 2**, which shows the oxide thicknesses of Zircaloy-4 and ZIRLO rods from multiple plants plotted as a function of MFDI. The data include oxide thickness measurements along the length of a fuel rod, not just the maximum thickness of the rod. The use of MFDI allows for a better comparison of oxide growth on rods from different plants, as it accounts for the thermal component to oxidation. Burnup is not a good metric for oxide thickness when one is comparing corrosion between plants operating at low and high temperatures. Such comparisons became more meaningful as utilities moved to more demanding fuel management schemes as reflected by increases in MFDI.

Table 1 Chemistries of zirconium alloys irradiated in pressurized water reactors to high burnup

Alloy	Nominal alloy composition (wt%)							
	Sn	Nb	Fe	Cr	Cu	V	Ni	O
Zircaloy-4	1.3		0.2	0.1				
E110		1.0						
E635	1.2	1.0	0.35					
ZIRLO	1.0	1.0	0.1					
Optimized ZIRLO	0.67	1.0	0.1					
M5		1.0						0.14
J-Alloys								
J1		1.8						
J2		1.6		0.1				
J3		2.5						
AXIOM alloys								
X1	0.3	0.7–1	0.05		0.12	0.2		
X2		1	0.06					
X4		1	0.06	0.25	0.08			
X5	0.3	0.7	0.35	0.25			0.05	
X5A	0.45	0.3	0.35	0.25				

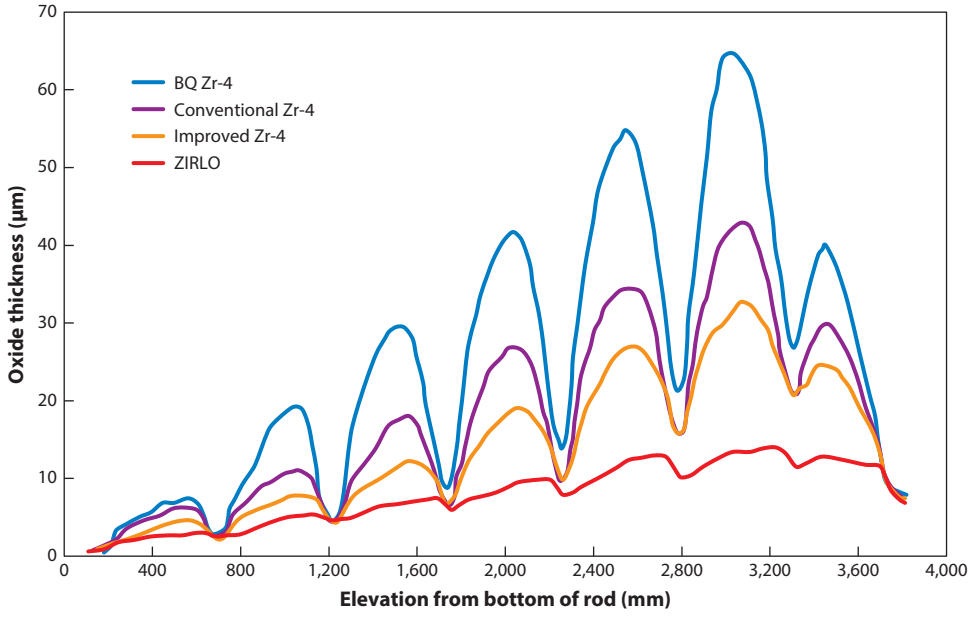

Figure 1

Axial variation of oxide thickness on zirconium alloy fuel rods. BQ Zr-4 is Zircaloy-4 that was processed with a beta quench near the final tube size, Conventional Zr-4 is Zircaloy-4 with 1.5% Sn, and Improved Zr-4 is Zircaloy-4 with 1.3% Sn. Zero elevation is the lowest point in the fuel assembly, at which the colder cooling water first comes in. Adapted from Reference 16.

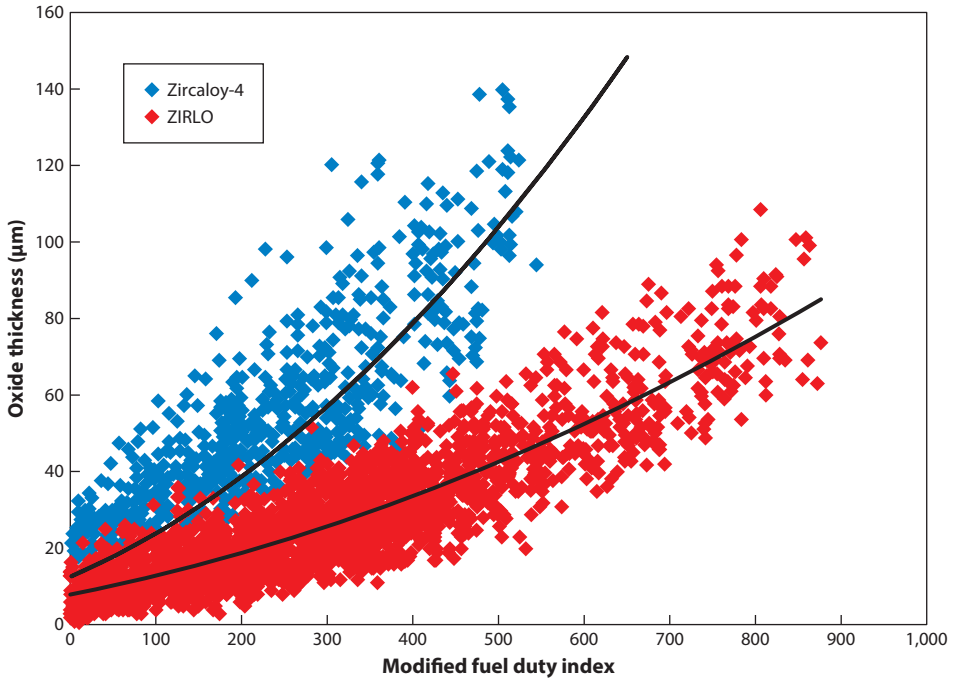

Figure 2

Comparison of Zircaloy-4 (*blue*) and ZIRLO (*red*) oxide thicknesses as a function of a modified fuel duty index. Adapted from Reference 17.

Following the introduction of ZIRLO, M5 was introduced as an advanced alloy in the early 1990s. The M5 alloy had a composition similar to that of E110, as it was nominally Zr–1% Nb. This alloy was a fully recrystallized ternary alloy of Zr-Nb-O with controlled levels of Fe and S (8, 18, 19). **Figure 3** compares the oxide thickness of M5 cladding with that of Zircaloy-4. The distinguishing feature of M5 is the lack of enhanced corrosion at burnups beyond 30 GWD/MTU (gigawatt-days per metric ton uranium). Throughout the 1990s and 2000s, ZIRLO and M5 became the dominant alloys for the replacement of Zircaloy-4 in PWRs.

Many factors determine corrosion. Fuel rod corrosion is primarily a function of time at temperature and only weakly a function of burnup, which helps explain the large spread in oxide thickness when plotted as a function of burnup. Factors such as coolant flow, coolant chemistry, fast flux, and cladding hydrogen levels can further enhance the sensitivity of corrosion to temperature variations. As mentioned above, the MFDI, although better than burnup at reducing the data scatter, does not account for all variables that contribute to cladding oxidation.

Alloy development efforts have continued with the introduction of Optimized ZIRLO, which is designed to retain the favorable properties of ZIRLO while improving corrosion resistance. In recognition of the positive corrosion benefit of reduced Sn content (20, 21), Optimized ZIRLO contains a nominal Sn level of 0.67% compared with the 1% level in ZIRLO. Optimized ZIRLO fuel rods have been irradiated to burnups in excess of 70 GWD/MTU, with oxide thickness approximately 40% lower than in ZIRLO, as shown in **Figure 4** (22). Enhancement of the corrosion of Optimized ZIRLO is delayed, with increases occurring between 40 and 50 GWD/MTU. Compared with ZIRLO, not only does Optimized ZIRLO show lower oxide thickness, but the data are from plants with higher fuel duty.

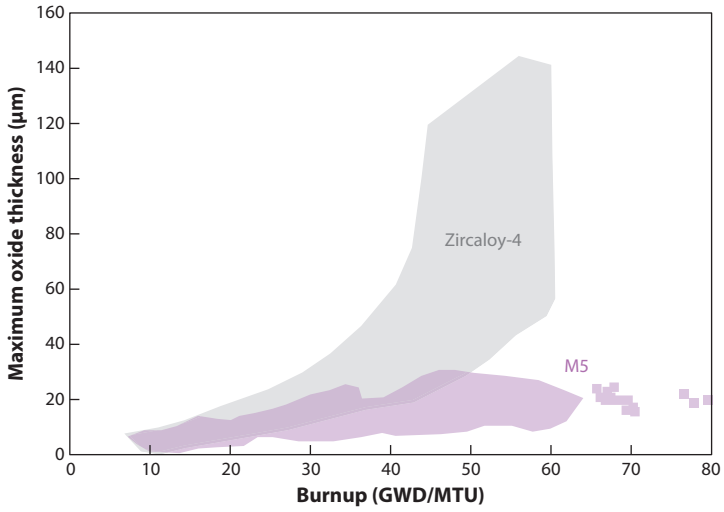

Figure 3

Burnup dependence of oxide thickness for M5. Adapted from Reference 25.

Additional alloy development programs have identified other alloy compositions that have significant improvements in corrosion performance following irradiation to high burnups. J-Alloy rods (J1 and J2) have achieved rod-averaged burnups of approximately 68 GWD/MTU following three cycles of irradiation (23). The alloys contain higher Nb levels than do E110 and M5, with one alloy (J2) containing a ternary addition of Cr. **Figure 5** shows peak oxide thickness. Similar to M5, the alloys do not exhibit the more rapid increase in oxide thickness exhibited in the Zircaloy-4 rods at burnups above 30 MWD/MTU.

AXIOM alloys have been irradiated to burnups greater than 70 GWD/MTU (20, 21, 24). The alloys contain between 0.3% and 1% Nb, with three of the five alloys containing low levels of Sn, as shown in **Table 1**. Oxide thickness measurements show a significant reduction in corrosion relative to ZIRLO, as shown in **Figure 8** (below). The improvement in corrosion performance is significant when plotted as the function of MFDI; a clear separation in performance is seen between AXIOM alloys and ZIRLO. There is no apparent enhancement in corrosion at burnups to 70 GWD/MTU.

Beginning with the introduction of ZIRLO in 1987, significant in-reactor corrosion experience regarding the behavior of new alloys has been achieved. Not only do the advanced alloys exhibit lower oxide thickness compared with that of Zircaloy-4, but the reactor environments are more demanding, with increased coolant temperature and longer cycle lengths. A challenge in the development of new alloys is identifying out-of-pile characterization that provides sufficient confidence to invest resources to put the alloys into a commercial reactor to obtain experience for licensing of the alloy.

One characteristic of the advanced alloys is lower corrosion rates when they are autoclaved in 360°C water. The correlation of autoclave performance and in-reactor performance was previously noted (16). This correlation is shown through comparison of autoclave results in **Figure 6*a*** and in-reactor oxide measurement in **Figure 1** (16). The additional autoclave results in **Figure 6** also show lower corrosion for M5, J-Alloys, and AXIOM alloys relative to Zircaloy-4 or ZIRLO. The results show that the initial transition in corrosion kinetics takes a long time, which is indicative

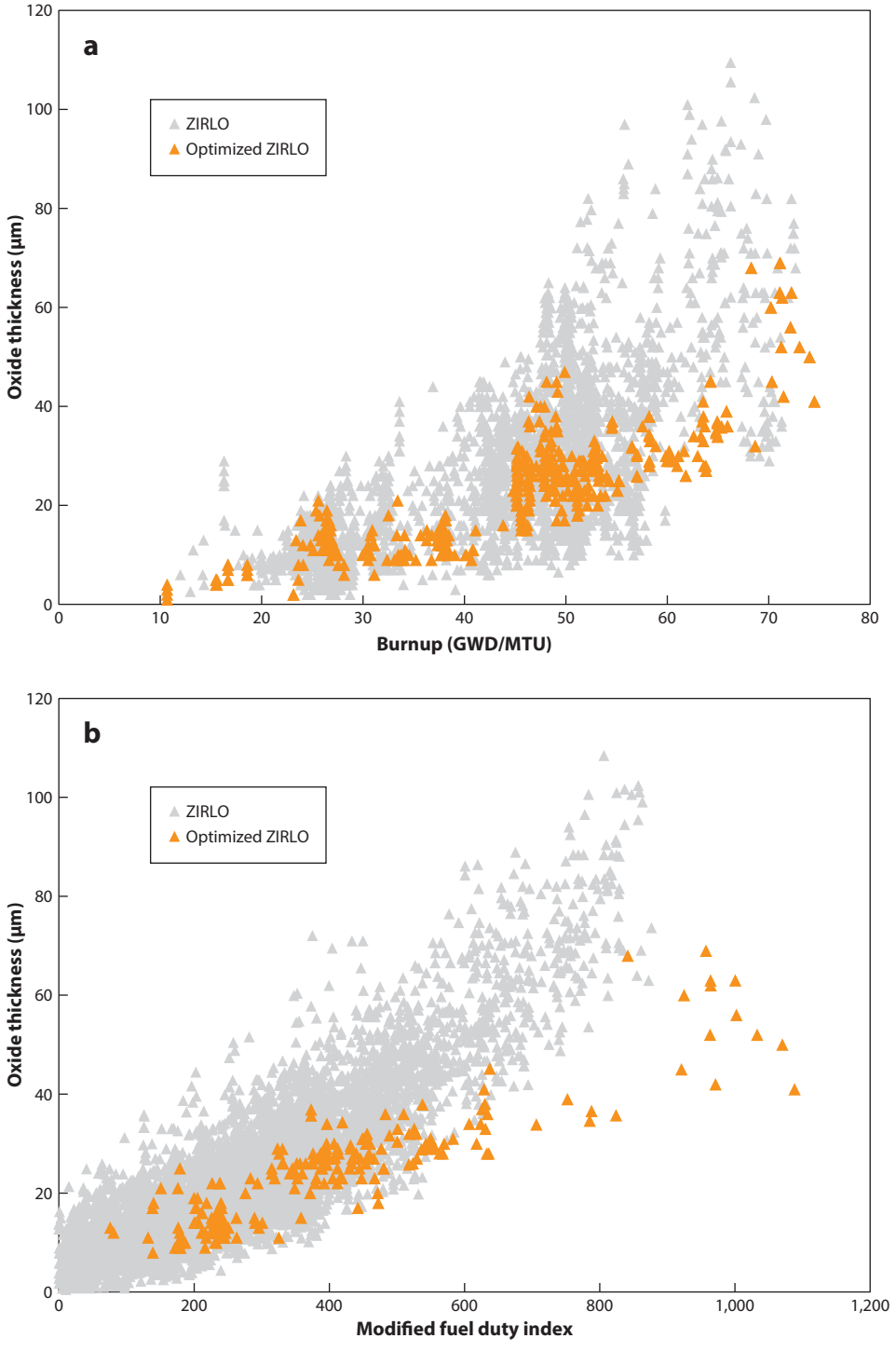

Figure 4

Improved performance of Optimized ZIRLO (*orange*) relative to ZIRLO (*gray*) (*a*) as a function of burnup and (*b*) as a function of modified fuel duty index. Adapted from Reference 20.

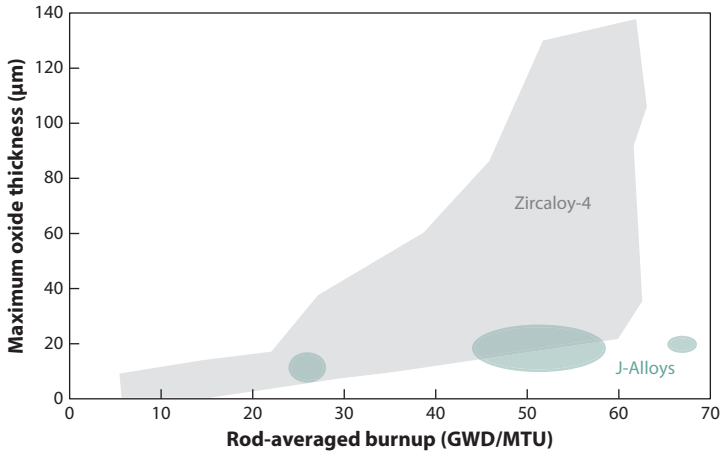

Figure 5

Oxide thickness of high-burnup J-Alloys versus rod-averaged burnup. Adapted from Reference 23.

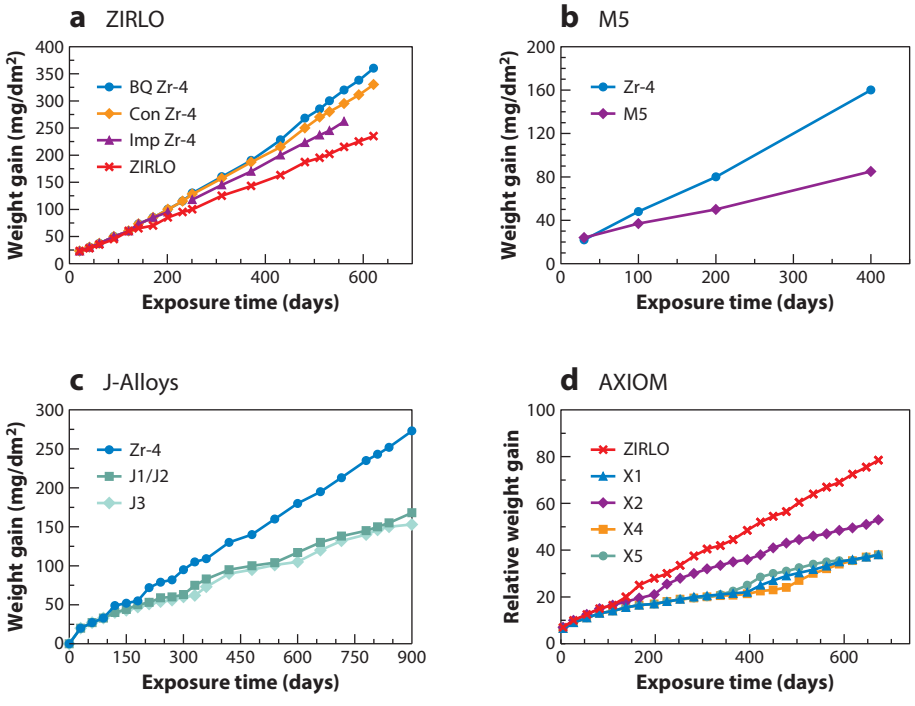

Figure 6

Autoclave results from testing of advanced alloys in 360°C water. BQ Zr-4 is Zircaloy-4 that was processed with a beta quench near the final tube size, Con Zr-4 is Conventional Zircaloy-4 with 1.5% Sn, and Imp Zr-4 is Improved Zircaloy-4 with 1.3% Sn. Panel *a* adapted from Reference 16; panel *b* adapted from Reference 25; panel *c* adapted from Reference 23; panel *d* adapted from Reference 24.

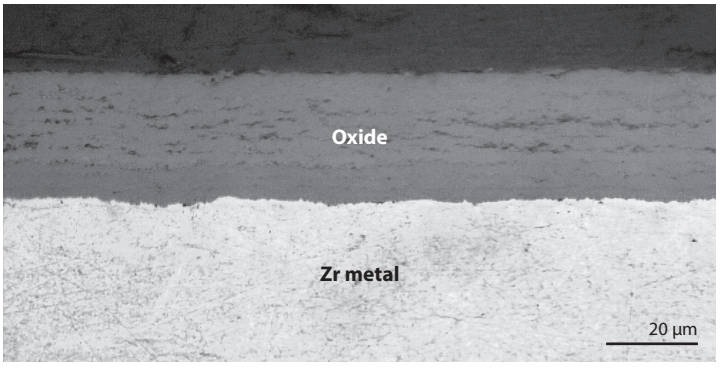

Figure 7

Periodic oxide layers in AXIOM X1 at 70 GWD/MTU.

of thicker periodic oxide layers and reduced posttransition corrosion rates. Such characteristics are also reflected by the lower in-reactor corrosion of the advanced alloys.

Although autoclave tests in 360°C water can show periodic growth of the oxide, they do not exhibit the enhanced corrosion observed on Zircaloy-4 at burnups above 30 GWD/MTU. Among the several proposed explanations for enhanced in-reactor corrosion are radiation enhancement from neutron flux, changes in microstructure such as dissolution of second-phase precipitates (SPPs), impact from formation of a hydride rim, and water chemistry. Although the explanations allow for correlations with the in-reactor behavior, it is not clear how those postulated causes can change the oxidation mechanism to result in enhanced corrosion with increased burnup.

Corrosion in 360°C water containing 70-ppm Li shows normal oxidation kinetics for ZIRLO along periodic oxide layers, whereas Zircaloy-4 and Zr–2.5% Nb exhibit accelerated oxidation and no periodicity in the oxide growth (26). The possible implication of this observation is that the enhanced corrosion in reactor may be a result of a breakdown of the periodic oxide growth. A micrograph of the oxide formed on a high-burnup protective alloy (AXIOM) shows periodicity in the oxide growth with regularly spaced cracks, as shown in **Figure 7**. Periodic oxide layers have also been observed on high-burnup M5 (127). These protective alloys (M5 and X1) show no enhanced oxidation with increasing burnup, as shown in **Figures 3** and **8*a***, respectively. Although testing in 360°C water appears to be a useful screening test to identify alloys with long pretransition times and low posttransition corrosion rates, good in-reactor performance requires that the periodic oxide growth of the oxide not be interrupted by the in-reactor environment. Understanding the reasons for the breakdown of the periodic growth of the oxide is an area of ongoing research.

3. THE BASIC CHARACTERISTICS OF ZIRCONIUM CORROSION

The corrosion reaction of zirconium metal in water is written as

$$Zr + 2H_2O \rightarrow ZrO_2 + 2H_2. \quad 1.$$

The two terms on the right-hand side of Equation 1 are the products of the reaction: the formation of an oxide layer and the generation of hydrogen, some of which gets picked up by the metal. The zirconium oxidation is driven by the high free energy of the zirconium oxide formation reaction [~965 kJ/mol at 360°C (27, 28)]. Because of the zirconium oxidation thermodynamics and the environment to which the material is exposed under operating conditions, electrochemical

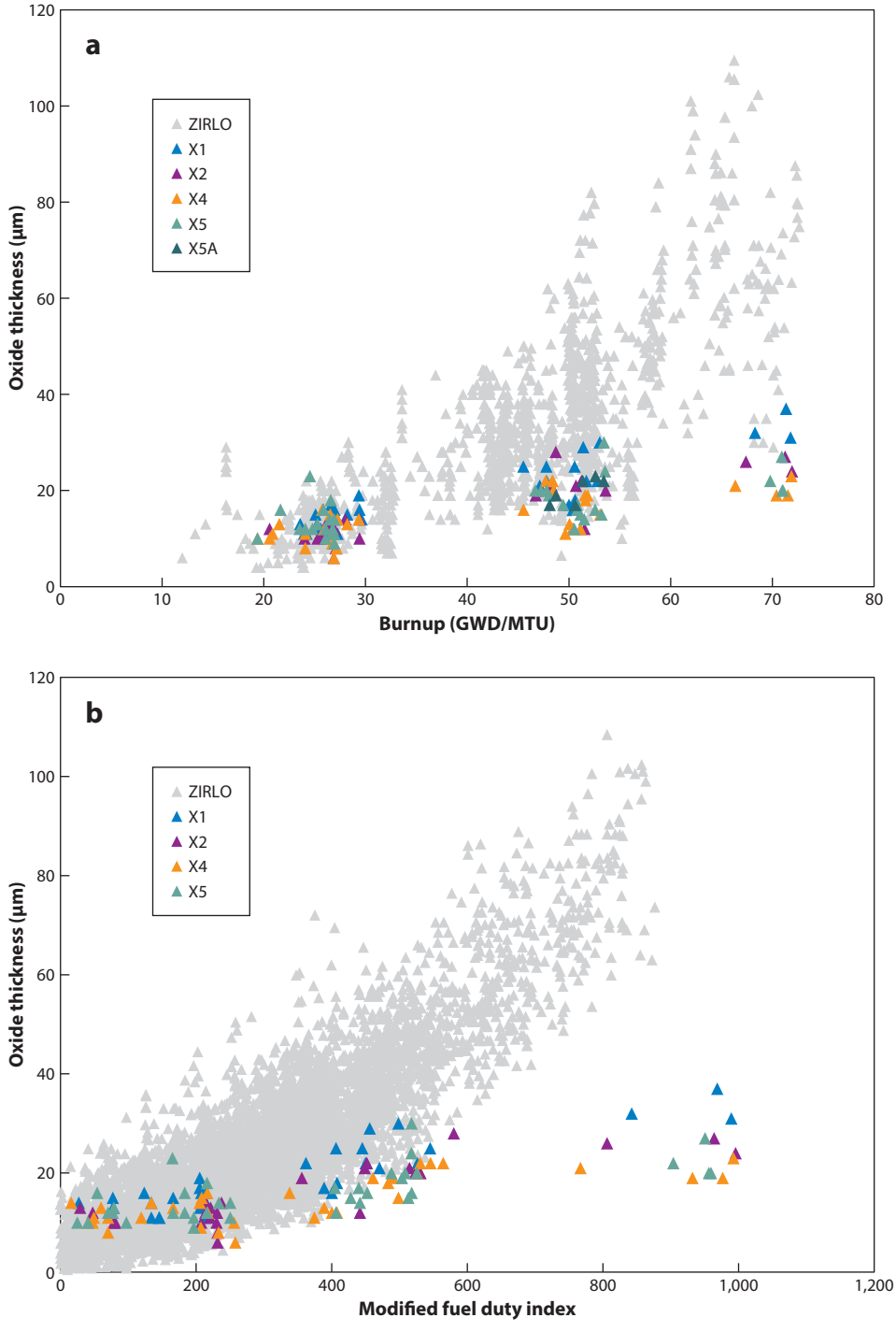

Figure 8

Improved performance of AXIOM alloys (*various colors*) relative to ZIRLO (*gray*) (*a*) as a function of burnup and (*b*) as a function of modified fuel duty index. Adapted from Reference 24.

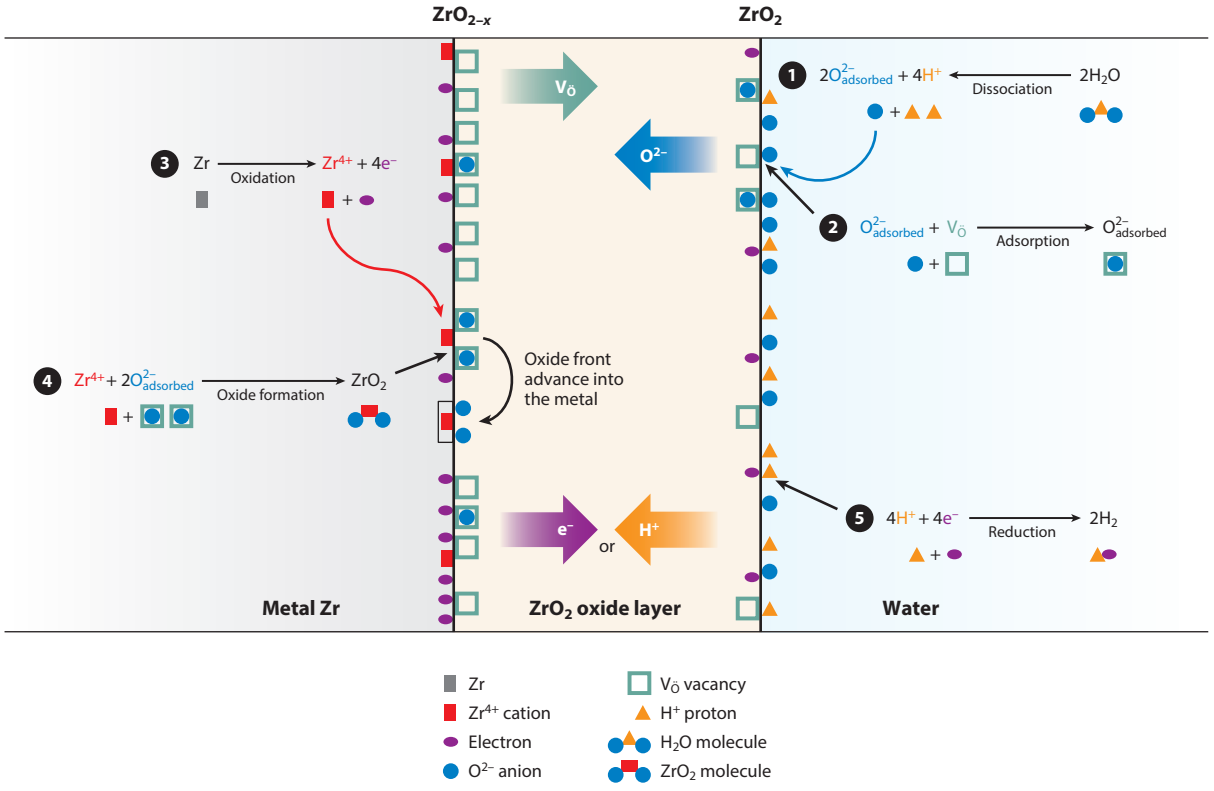

Figure 9

Schematic of the corrosion process in zirconium alloys. Surface reactions 1–5 occur in series, but the rate-limiting steps are the transport of oxidizing species (oxygen, electrons, and hydrogen) in the oxide layers, as indicated by the thick arrows.

potentials are established at the oxide layer (oxide/water and oxide/metal) interfaces, driving the transport of atomic species across the oxide film.

The oxidation process of zirconium alloys in the presence of a protective oxide layer can be conceptually divided into several steps, as reviewed in Reference 29. **Figure 9** shows a schematic of the process. First, oxygen in the water molecule dissociates and is adsorbed onto the oxide layer surface at an oxygen vacancy site. Because of the defect concentration gradient [the oxide is substoichiometric at the oxide/metal interface (30)] and the electric potential across the oxide [resulting from ambipolar diffusion (31) and the space charge in the oxide (32, 33)], the oxygen anions diffuse either through the bulk of the oxide or along the oxide grain boundaries via solid-state diffusion (34, 35). When the oxygen anion reaches the oxide/metal interface, it reacts with zirconium cations to form new oxide. The formation of this new oxide releases electrons, which then migrate through the oxide by a hopping mechanism to reduce the hydrogen ions at the cathodic site (36). Whether the location of the cathodic site is at the oxide/water interface, within the oxide, or at the outer surface of the protective layer is unknown. Some hydrogen atoms do not recombine with electrons at the oxide/water interface but are instead absorbed by the oxide layer and make their way into the metal. This phenomenon is termed hydrogen pickup. These atoms diffuse through the oxide layer to the metal, where they are found either in solid solution in the α-Zr matrix or, if the hydrogen concentration is high enough, as hydride precipitates (37).

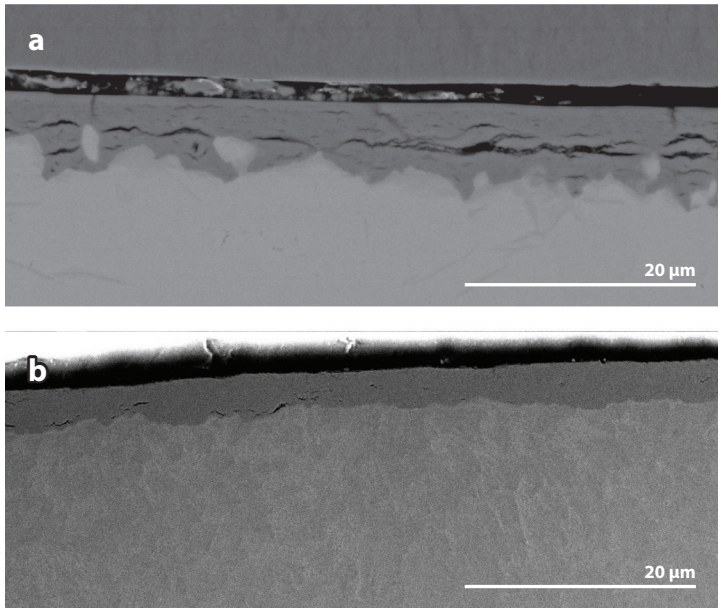

Figure 10

SEM micrographs of oxide formed in 360°C water. (*a*) Sponge zirconium after 69 days of exposure. (*b*) Zircaloy-4 after 75 days of exposure.

3.1. Oxide Stability

As mentioned above, the corrosion of pure-zirconium samples produces an unstable corrosion process, in which the oxide/metal interface constantly breaks down and the oxide layer advances very rapidly and unevenly into the metal. **Figure 10*a*** shows a cross-sectional micrograph of an oxide layer formed on sponge zirconium after 69 days of exposure in 360°C water in an autoclave (38). The oxide is extensively cracked and nonprotective, and the oxide layer advances unevenly, with likely preferential attack along the metal grain boundaries. In contrast, the oxide formed in an alloy such as Zircaloy-4 is protective and grows stably. **Figure 10*b*** shows an oxide layer formed on Zircaloy-4 after a 75-day exposure to 360°C water in an autoclave. Compared with the case for the sponge zirconium sample, the oxide growth in Zircaloy-4 is much more stable, and the rate is considerably lower, as shown by the smaller oxide layer thickness.

Thus, the zirconium oxide formed on zirconium alloys is mostly protective. After oxide layer formation, direct contact between the metal and the water no longer exists, thereby preventing the corrosion reaction from happening directly. Instead, the oxidizing species have to diffuse through the oxide layer. Observation of the zirconium oxide system at normal operating temperatures has confirmed that zirconium oxide is an *n*-type semiconductor (39, 40) and that the oxide growth occurs by oxygen anion migration through the oxide film, with the formation of new oxide taking place at the metal/oxide interface (41, 42).

3.2. General Observations

A few general characteristics of the waterside corrosion and associated hydrogen pickup of zirconium alloys that exhibit growth of protective oxides should be taken into consideration.

1. The corrosion mechanism involves the formation of a protective layer through which the corrosion species must travel to continue corrosion. The fact that the corrosion rate decreases

with increased exposure (and thus with oxide thickness) means that transport of corrosion species through the layer is the rate-limiting step for the overall reaction.

2. A protective oxide such as that shown in **Figure 10*b*** is adherent and exhibits a black shiny appearance, whereas a nonprotective oxide is white, nonadherent, and flaky. Interestingly, when the weight gain is measured after a corrosion exposure, the oxide thickness corresponds, within experimental error, to the calculated oxide thickness, assuming that all the weight gain is oxygen and is used to form ZrO_2. This agreement indicates that the volume expansion attendant upon the transformation of $Zr \rightarrow ZrO_2$ (the Pilling-Bedworth ratio is 1.56) occurs almost totally in the oxide growth direction; that is, the consumption of 1 μm of zirconium alloy metal results in the creation of a 1.56-μm-thick oxide.
3. The evidence also shows that, unlike the case for steels, in which both iron and oxygen migrate, only oxygen moves during waterside corrosion of zirconium alloys (41).
4. In a given environment, the corrosion rate is a characteristic of each zirconium alloy, with good reproducibility from sample to sample. The pretransition corrosion rate in the oxidation kinetics is well described by an empirical law of the form

$$w = At^n, \qquad 2.$$

where w is the weight gain [normally in milligrams per (decimeters squared)], t is the exposure time, and A and n are constants. The value of n in particular is characteristic of each alloy (16, 38). **Figure 11** shows the pretransition corrosion kinetics of ZIRLO; the data are well fit by Equation 2.

5. Another feature of oxide growth exhibited by alloys is the oxide transition, in which the corrosion rate suddenly increases, as if it were returning to the start of the corrosion process and reproducing the initial corrosion kinetics. **Figure 12** shows transmitted light optical micrographs showing the transition layers of three alloys: Zircaloy-4, ZIRLO, and Zr–2.5% Nb (43). The transition thickness is constant but different for each alloy. The Zircaloy-4 oxide layer shown in **Figure 12*b*** exhibits 17 transition layers of equal thickness. This evidence suggests that the structure of the oxide layer plays a role in determining corrosion kinetics.
6. Each alloy has a different hydrogen pickup fraction during corrosion. For example, the hydrogen pickup fraction of Zircaloy-2 is higher than that of Zircaloy-4. As seen below, the hydrogen pickup fraction also changes during corrosion.

3.3. Corrosion Kinetics

Because of the difficulty and expense of handling irradiated materials, most zirconium alloy corrosion studies are performed on specimens that are autoclaved in test environments ranging from high-temperature water or steam to simulated LWR chemistry such as water containing Li, B, and dissolved H for assessment of materials for PWR application. The use of autoclave experiments has significantly increased the diversity of alloys that have been studied. As stated above, very small additions of alloying elements can significantly change the oxidation kinetics of zirconium alloys from immediate breakaway to genuine protective behavior, as shown by the corrosion behaviors depicted schematically in **Figure 13** and reported in Reference 38.

As described above, the corrosion kinetics of zirconium alloys in aqueous solutions is usually described as an initial pretransition regime with an approximate parabolic or subparabolic oxidation rate, followed by the oxide transition, defined as the oxide thickness at which the change in corrosion kinetics occurs. This change usually occurs at an oxide thickness of 2 to 3 μm.

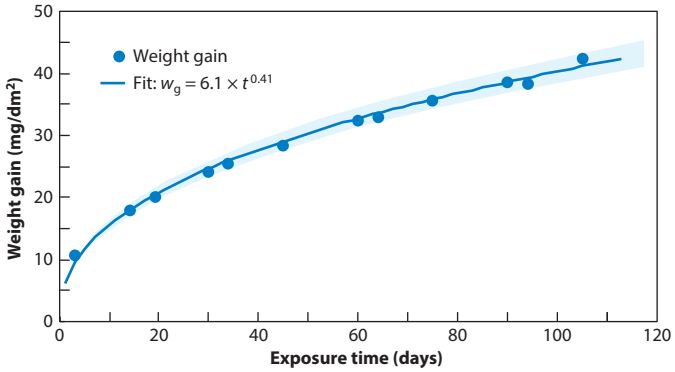

Figure 11

Power-law fit of the pretransition regime of the ZIRLO sheet alloy. The light blue–shaded area on the plot represents the error associated with the power-law fit to enclose all experimental data points and is equal to ± 5% in this case.

Not all zirconium-based alloys follow this oxidation behavior. Whereas protective oxides such as those formed on Zircaloy-4 follow this cyclical behavior, other alloys can show initial protective behavior followed by a rapid acceleration of the weight gain with no recovery: This phenomenon is termed corrosion breakaway. When breakaway occurs, the oxide turns white, which is characteristic of a porous, nonprotective, stoichiometric ZrO_2, and oxide spallation can occur. Breakaway corrosion can be thought of as an oxide transition in which the newly formed oxide is no longer protective so that the corrosion rate remains high. Some models have been proposed (44–47), but a complete understanding of the oxide transition and of the parameters leading to breakaway is still lacking.

3.4. Effect of Alloying Elements on Oxidation Kinetics

In the protective regime, the corrosion rate of zirconium alloys decreases as the thickness of the oxide layer increases (48). It is generally considered that the diffusion of charged species (electrons and oxygen vacancies) under a concentration gradient controls the oxidation mechanism (11, 49, 50). This assumption leads to the Wagner parabolic scaling law for the oxidation kinetics, shown in Equation 2, with $n = 0.5$ (51, 52). However, oxidation of zirconium alloys is frequently subparabolic ($n < 0.5$) (11, 38, 53–55). The exponent n has been carefully measured in various zirconium alloys at the beginning of the corrosion by fitting weight gain data as a function of exposure time to a power law (38, 54, 56). It is usually found that n is closer to parabolic for Nb-containing alloys and is closer to cubic ($n = 0.33$) or even quadratic ($n = 0.25$) and lower for Zircaloy-type alloys. This subparabolic behavior is not common in metal oxidation for oxide layers of the micrometer scale (51). Importantly, even if the subparabolic nature of n may not be directly derivable from a given metal oxidation theory, it nevertheless represents clear phenomenological evidence of a deviation from the Wagner oxidation mechanism (31, 57).

3.5. Hydrogen Pickup Fraction

To compare the hydrogen pickup of different alloys, it is necessary to quantify the amount of hydrogen picked up relative to the amount of corrosion. To this end, the hydrogen picked up by the metal during reactor or autoclave exposure is measured and normalized to the total hydrogen

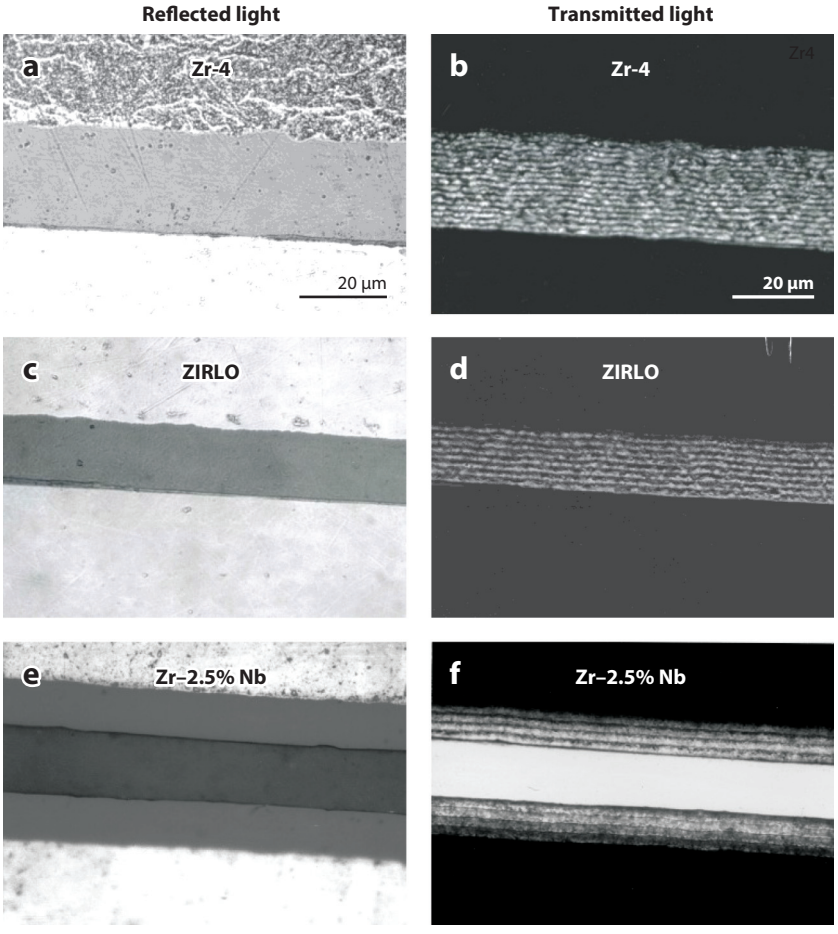

Figure 12

Optical micrographs of oxide layers formed on (*a*,*b*) Zircaloy-4 (Zr-4), (*c*,*d*) ZIRLO, and (*e*,*f*) Zr–2.5% Nb. Adapted from Reference 41.

generated in the corrosion reaction (58). Indeed, only the hydrogen generated by the corrosion reaction is susceptible to entering the metal (59). Thus, the total hydrogen pickup fraction f_{H}^{t} is defined as the ratio of the hydrogen absorbed from the beginning of the corrosion test to the total amount of hydrogen generated by the corrosion reaction up to that time. Conversely, the instantaneous hydrogen pickup fraction f_{H}^{i} is defined as the ratio of (*a*) hydrogen absorbed into the cladding from time t to time $t + \Delta t$ to (*b*) the total amount of hydrogen generated by the corrosion reaction in the interval Δt:

$$f_{\mathrm{H}}^{t} = \frac{\Delta_0^t \mathrm{H}_{\mathrm{absorbed}}}{\Delta_0^t \mathrm{H}_{\mathrm{generated}}}, \quad f_{\mathrm{H}}^{i} = \frac{\frac{\mathrm{dH}_{\mathrm{absorbed}}}{\mathrm{d}t}}{\frac{\mathrm{dH}_{\mathrm{generated}}}{\mathrm{d}t}} \sim \lim_{\Delta t \to 0} \frac{\Delta_t^{t+\Delta t} \mathrm{H}_{\mathrm{absorbed}}}{\Delta_t^{t+\Delta t} \mathrm{H}_{\mathrm{generated}}}. \qquad 3.$$

The hydrogen pickup fraction varies from alloy to alloy. It has been measured as being as high as 80% for Ni-containing alloys to as low as 5–10% for Nb-containing alloys (56, 60). The f_{H}^{t} for Zircaloy-4 is usually approximately 20–25%, whereas f_{H}^{t} for ZIRLO is approximately 15% (61).

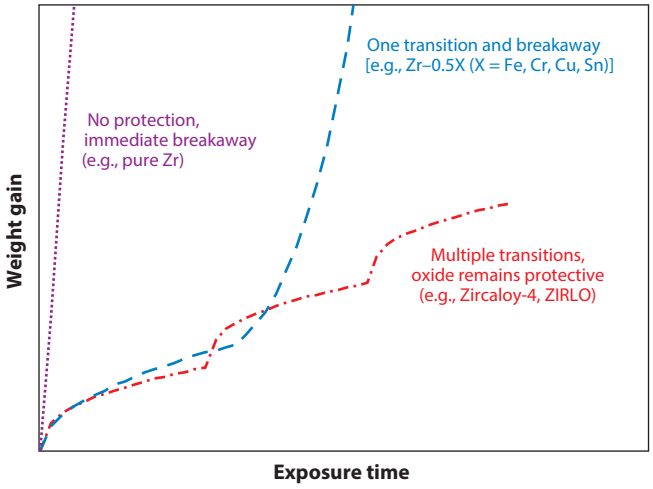

Figure 13

Schematic representation of the corrosion of zirconium alloys.

For two reasons, it is believed that the hydrogen enters the oxide in the form of protons rather than hydroxide ions. First, if only OH^- entered the oxide, f_H^t would never be greater than 50%, which is in contradiction with experimental observations (56). Second, anodic polarization decreases (whereas cathodic polarization increases) the rate of hydrogen absorption, suggesting that charged hydrogen species, and not neutral hydrogen, are part of the hydrogen uptake process (62–64).

4. OXIDE MICROSTRUCTURE AND CORROSION MECHANISM

The detailed study of oxide layer microstructure has yielded considerable insights into the growth mechanism of oxide layers in zirconium alloys when exposed to high-temperature water. In alloys that form a protective oxide layer in such conditions (as is the case with all commercial alloys used in the nuclear power industry), the oxide growth is stable, the oxide is adherent, and no evidence of meaningful dissolution of the outer oxide is seen (as mentioned above, the weight gain corresponds almost exactly to the corrosion layer thickness).

4.1. Oxide Growth and Texture Formation

Microstructure examination shows that oxidation starts by the formation of small, equiaxed oxide grains on the metal, as verified by the consistent observation of small oxide grains near the oxide/water interface (65). These small oxide grains are more or less randomly oriented and exhibit a mix of tetragonal and monoclinic ZrO_2 crystal structures. As the grains grow, they become columnar so as to favor the growth of properly oriented grains to minimize the stress accumulation [as stated below, the oxide/metal interface is oriented at a small angle from the $(200)_M$ plane,[2] which exhibits the highest elastic constant]. Out of this initial collection of small grains, only a few are properly oriented for columnar growth, which means that only a small fraction of the grains grow into columnar grains. The transition from equiaxed to columnar growth occurs at a diameter of

[2]Note that the designation of the monoclinic planes used here follows PDF# 37-1484, in which a = 0.5313 nm, b = 0.5213 nm and c = 0.5147 nm.

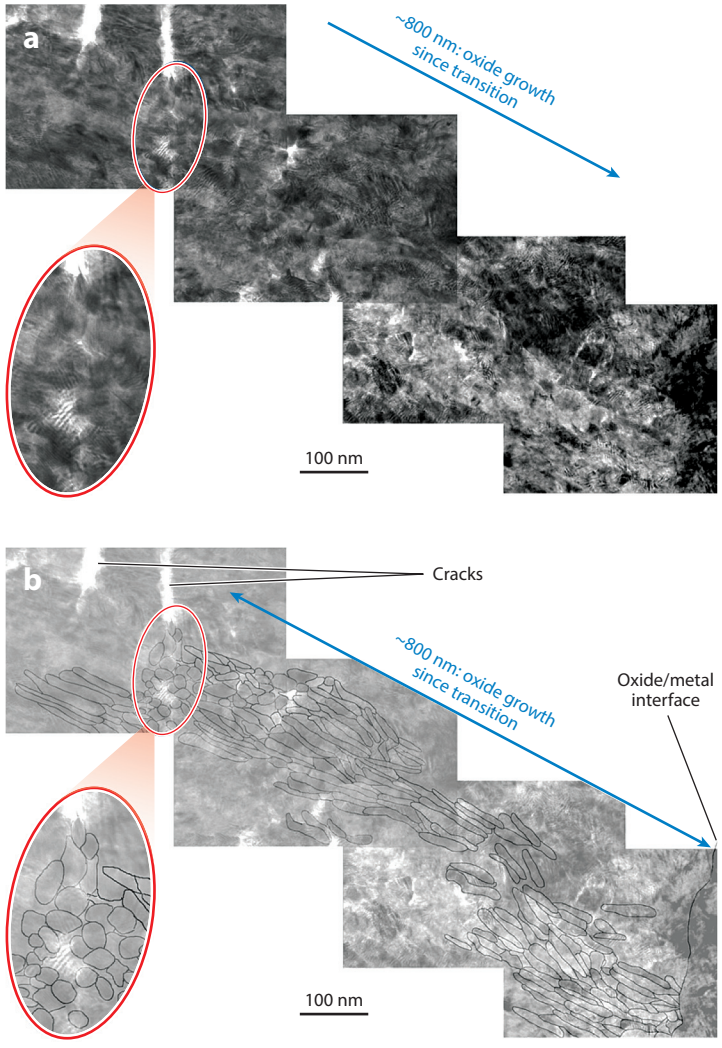

Figure 14

(*a*) Cross-sectional electron micrograph showing columnar oxide structure and equiaxed oxide grains present in the oxide layer at the time of the transition (see text). (*b*) Schematic drawing of microstructure to more clearly show grain structure. Adapted from Reference 96.

approximately 30–40 nm, which is also the diameter at which the stable monoclinic phase becomes favored over the tetragonal phase. The columnar grains grow to a length of approximately 200 nm, at which point grains normally have to renucleate to maintain the proper orientation. This anisotropic columnar growth results in a fiber texture, with an actual oxide orientation that various researchers have ascribed to $\bar{2}01$, $\bar{4}01$ and $\bar{6}01$ (66, 67). **Figure 14** shows a transmission electron microscopy (TEM) micrograph of a cross-sectional sample of an oxide layer formed on Zircaloy-4. This micrograph shows the variation in oxide microstructure, with long, columnar oxide grains formed in between transitions and small, equiaxed grains formed at the beginning of the corrosion process and at the oxide transition.

4.2. The Oxide Transition

As the oxide grows, stresses accumulate in the oxide layer from the imperfect accommodation of the volume expansion associated with oxidation. Because this process occurs at different rates for different alloys, different transition thicknesses result. In-plane stresses on the order of 1–3 GPa have been measured in growing oxide films at various stages of film growth (67, 68). In parallel, oxide porosity develops in the layer, as revealed by Cox (69) and Cox & Yamaguchi (70) and more recently by Ni et al. (71, 72). This porosity takes the form of small tubes near or at the columnar oxide grain boundaries. The pores first start out as equiaxed cavities and grow into tubes as the oxide grows, as has been shown by TEM (73) and by tests performed in deuterated water (74). The increasing stress eventually causes lateral cracks to form, which causes an interlinkage of the porosity from the oxide/metal to the oxide/water interface, thus providing easy access to the water, which in turn increases the corrosion rate. The sudden nature of the transition is then related to the sudden oxide breakup after the stress reaches a critical value; the interlinkage of pores explains how lateral cracks can cause an overall loss of protectiveness. This is thought to be the mechanism related to the oxide transition (38).

In this scenario, the different transitions between alloys would result from a different rate of stress accumulation as the oxide grew; the idea is that different alloys would cause the volume expansion to be accommodated slightly differently, resulting in different levels of stress accumulation such that the oxide transition occurred at different times. The question of how the different alloys cause a differentiated accommodation of strains that results in different stress accumulations and different transition times has yet to be elucidated, although there have been various measurements of stress in growing oxides (67, 68, 75–77). These measurements are fraught with the problem of stress relief during cooldown [although a study has indicated that this problem may not be serious (76)] or during sample preparation, especially of cross-sectional samples. In addition, stress measurements are often achieved by measuring elastic strain, which can also occur because of other factors such as compositional variations, and the stress is often averaged over the oxide layer, although the stress is likely higher near the oxide/metal interface. Greater understanding is sorely needed in this area.

Once the corrosion rate increases, the protective layer reforms, and the process repeats periodically. As shown in **Figure 12**, the rate of repetition is very regular, which is a characteristic of the alloy, and such repetition can occur for many cycles.

4.3. Second-Phase Precipitates

The oxidation of SPPs [e.g., $Zr(Cr,Fe)_2$ in Zircaloy-4, β-Nb and ZrNbFe precipitates in ZIRLO] is delayed relative to that of the Zr matrix so that the precipitates are initially incorporated in metallic form into the oxide layer. This delayed oxidation of alloying elements incorporated into the oxide layer has been verified by TEM (78–80), by X-ray absorption near-edge spectroscopy (XANES) (81–83), and more recently by μ-XANES (29, 84). As the oxide advances further, the alloying elements in these precipitates eventually become oxidized; the delay is proportional to the tendency of elements to oxidize as specified by Ellingham's or Pourbaix diagrams. The oxide formed at the site of the former ZrCrFe precipitates is clearly much more fine grained than the bulk oxide and contains a larger percentage of the tetragonal phase. Various researchers have pointed to SPPs as possible cathodic sites for the corrosion reaction; as possible short-circuit paths through the protective oxide, either on their own or due to nearby cracking; as possible places for hydrogen storage; and as possible sources of stress in the oxide layer upon delayed oxidation. The specific role of SPPs in establishing the corrosion rate or in determining oxide breakup has not

been clarified. Given the inhomogeneous distribution of these precipitates in the oxide layer, any such model or mechanism will likely be complex.

4.4. The Tetragonal-to-Monoclinic Transformation

There has been much discussion in the literature regarding the potential role of the tetragonal oxide phase or the tetragonal-to-monoclinic phase transformation in the generation of stresses in the oxide and in the onset of oxide transition. The tetragonal content is normally quantified using the Garvie-Nicholson formula (85):

$$f_T = \frac{I^t_{101}}{I^m_{\bar{1}11} + I^t_{101} + I^m_{111}}, \quad 4.$$

where I^t_{101} is the intensity of the 101 tetragonal peak and $I^m_{\bar{1}11}$, I^m_{111} are the intensities of the respective monoclinic peaks; maximum values of f_T ranging from 5% to 50% have been reported using synchrotron X-ray diffraction (55, 67, 86), with the highest levels near the oxide/metal interface. A high tetragonal content has been associated both with protective behavior and with loss of protectiveness (88). The protective oxide has often been associated in the literature with the tetragonal phase, and the protective fraction is sometimes termed the tetragonal oxide. Our view is that there is little evidence that the tetragonal phase content plays any significant role in the oxide development; its observation in the protective oxides is a result of correlation rather than causation. The presence of tetragonal oxide may indicate other phenomena (such as stress level or grain size), but no credible mechanism that directly relates tetragonal phase content to specific corrosion behaviors has been proposed.

4.5. The Structure of the Oxide/Metal Interface

The ZrO phase diagram predicts an equilibrium between ZrO_2 and Zr at the oxide/metal interface with approximately 28-at% O in solid solution (89). In reality, such an equilibrium is never established, as the oxide/metal interface constantly moves into the metal during oxidation and thus consumes the metal nearby. However, the metal region near the oxide/metal interface is clearly different from the rest of the metal, with several metastable phases reported, including an amorphous phase (90), the omega phase (91), ZrO (92), Zr_3O followed by Zr–30% O (43, 80), and a sequence of phases by atom probe (93).

Figure 14 shows a TEM micrograph of the oxide structure. The oxide structure shows well-aligned columnar grains, with equiaxed grains both at the interface and at the location of the transition. The sequence of phases formed is shown in **Figure 15**, which illustrates a cut through an atom probe needle and the various phases ahead of the moving oxide front. The oxide layers when studied in cross section can be seen as geological strata, in which different structures were formed and deposited at different times; thus, by walking back from the oxide/metal interface and knowing the corrosion kinetics, one can determine when the transition occurred and relate the corrosion kinetics and the occurrence of the transition to oxide features.

Recent studies that combined TEM using EELS and atom probe applied to the same oxide layers at different oxidation stages have indicated that all these phases may form at different times of the corrosion process (94–96). Three different phases are seen at the oxide/metal interface during the pretransition period: (*a*) a small intermediate layer identified as a cubic ZrO phase; (*b*) blocky grains found at some places along the interface, with diffraction patterns indexed as Zr_3O; and (*c*) an oxygen-saturated suboxide layer in the metal. The width of these interfacial regions decreases markedly at transition, likely because the high corrosion rates at transition do not allow them time to form. This interfacial region is much thicker during high-temperature (500°C) corrosion (97).

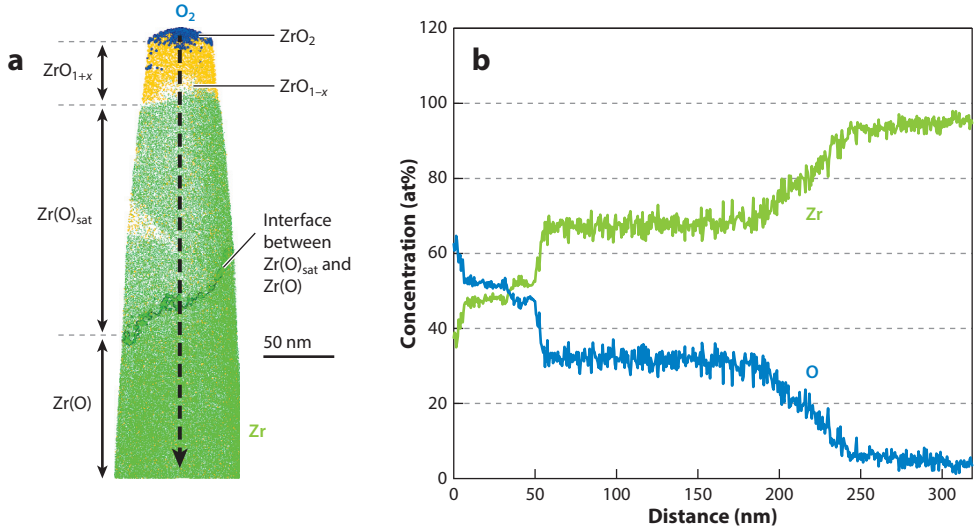

Figure 15

(*a*) Atom probe analysis of the oxide/metal interface for Zircaloy-4 corrosion. (*b*) Line profile of oxygen and zirconium concentrations ahead of the oxide front. Adapted from Reference 95.

4.6. Summary of Oxide Structure

Although much knowledge has been gained about the structure of these oxide layers, the central question of how alloying elements cause oxide growth stabilization is still unanswered. Possible hypotheses invoke grain boundary chemistry in the alloys that is different from that in pure Zr or different growth rates for different grain orientations (11; B. Cox & A.T. Motta, private communication). The alloying elements are clearly associated with different pretransition oxidation kinetics, as characterized, for example, by the value of n. As is shown below, the pretransition kinetics may be related to the conductivity of the oxide and hydrogen pickup.

Moreover, alloys have a very well defined transition thickness. Because the corrosion rate increase upon transition is sudden, a mechanism of loss of protectiveness that occurs fairly rapidly must be invoked. Two main mechanisms have been considered in the literature: (*a*) stress accumulation leading to oxide breakup and consequent easy access of water to the oxide/metal interface and (*b*) the development of oxide porosity that percolates (forms a continuous path through the layer) at a critical pore density and allows for access of water to the oxide/metal interface.

In the first case, the different transition thicknesses of different alloys could be explained by the different rates of stress accumulation. In this circumstance, the stress accumulation would be caused by small variations in the strain tensor of the $Zr \rightarrow ZrO_2$ transformation, resulting in larger or smaller lateral strains and in corresponding variations in the in-plane stresses, which would in turn lead to earlier or later oxide layer cracking and loss of protectiveness. One difficulty is that, although vertical cracks are necessary for water access, in-plane stresses create horizontal cracks, which are in fact observed.

In the second case, the different transition thickness may be explained by the different rates of porosity accumulation in oxides formed in different alloys. Such porosity may start as equiaxed and may eventually coalesce into long pore tubes. If it interlinked to the interface, a percolation condition would occur, with consequent water access to the oxide/metal interface. Ni and coworkers (71) provided evidence for such a mechanism of porosity growth and interlinkage. Deuterium

uptake experiments also show that the rate of porosity formation increases just before the transition (72). This evidence of pore formation and growth as an explanation of transition, however, does not explain why stress in the oxide decreases at transition.

A combination of the two hypotheses appears to be the most likely explanation. Porosity develops but does not reach a percolation condition, and once lateral cracking occurs as a result of a critical level of stress, the interlinkage of porosity then occurs, which causes easy access of water to the oxide/metal interface, triggering the transition (38).

5. HYDROGEN PICKUP DURING CORROSION

The hydrogen pickup fraction expresses a relationship between oxidation kinetics and hydrogen pickup. **Figure 16** shows the hydrogen pickup fraction (both total and instantaneous, as defined in Equation 3) for a ZIRLO sample subjected to corrosion testing at 360°C for 240 days. **Figure 16*a*** shows the corrosion weight gain and hydrogen content, whereas **Figure 16*b*** and **Figure 16*c*** show the total hydrogen pickup fraction and instantaneous hydrogen pickup fraction, respectively. The pickup fraction is clearly not constant throughout the corrosion process, because if it were, the hydrogen content curve in **Figure 16*a*** would have the same shape as the corrosion kinetics curve. This lack of direct relationship between corrosion and hydrogen pickup is also reflected in **Figure 16*c***, which plots the hydrogen pickup fraction versus exposure time. **Figure 16*c*** clearly shows that the pickup fraction increases just before the oxide transition and that the overall pickup fraction in the second cycle is higher than in the first cycle (56).

As stated above, some general observations can be made concerning hydrogen pickup in zirconium alloys.

1. The hydrogen enters the oxide under the form of protons (98, 99).
2. f_H^t decreases with Nb additions, and the oxidation kinetics of Nb alloys is more parabolic compared with that of Zircaloy-type alloys.
3. f_H^i varies as a function of oxide thickness. After a first rapid increase, f_H^i stabilizes once the oxide thickness reaches 30% to 70% of the oxide transition thickness. Then f_H^i increases significantly before dropping just before the oxide transition. These variations repeat in the next transition regime following oxidation kinetic periodicity.

These observations concerning hydrogen pickup mechanism are applicable to most of the investigated zirconium alloys.

The effects of precipitate size and volume fraction are not well understood (63, 100), but for a given precipitate volume fraction, an increase in the number of precipitates (and thus a reduction of their sizes) increases f_H^t, possibly because more cathodic sites are available (56, 101). There is evidence that f_H^t depends strongly on the alloying element additions (102, 103), on the alloy microstructure and microchemistry (60, 100), and on the corrosion conditions (104). The addition of alloying elements generally decreases hydrogen pickup, with the exception of Ni, which increases pickup, and Sn, whose effect is not well determined (102, 105). Additionally, f_H^t increases from the initial pretransition regime through subsequent transitions, at least up to the third transition (50, 56, 106, 107).

Thus, there is evidence that f_H changes during the corrosion process such that different fractions of hydrogen are picked up at different stages of oxide film growth (106). Recent studies have shown that hydrogen pickup fraction evolution is periodic following the oxidation periodicity, but with a different time dependence (56, 106).

It is important now to address the specific relationship between hydrogen pickup fraction and oxidation kinetics. The hydrogen pickup fraction varies as a function of exposure time and presents

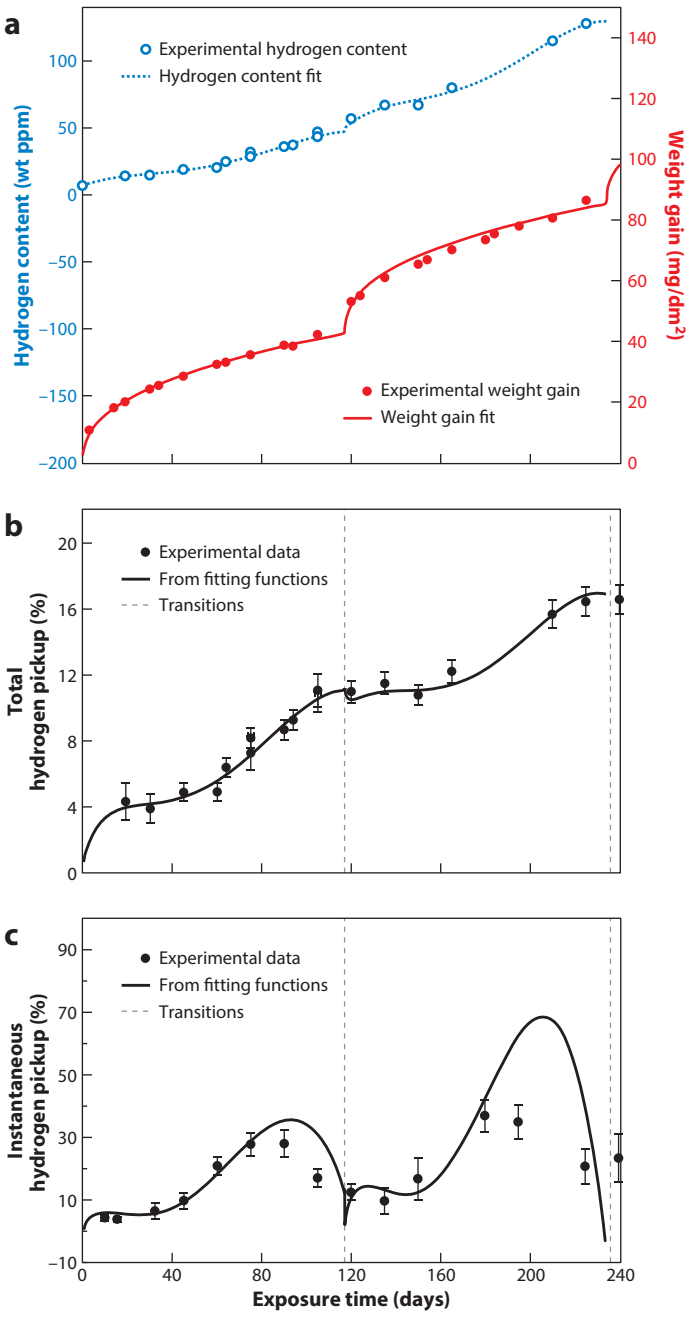

Figure 16

(*a*) Experimental weight gain (*red*) and hydrogen content (*blue*) as functions of exposure time and their fits. (*b*) Total hydrogen pickup fraction. (*c*) Instantaneous hydrogen pickup fraction and the functions derived from the weight gain and hydrogen content fits for ZIRLO.

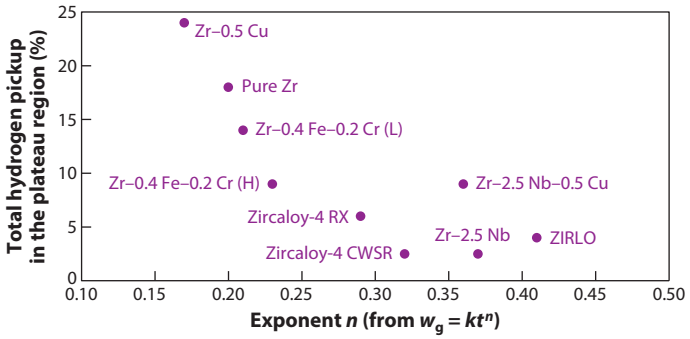

Figure 17

Total hydrogen pickup fraction in the plateau region as a function of the exponent n from the power-law fit of the weight gain $w = At^n$ for various zirconium alloys. CWSR indicates cold-worked stress relieved.

a general trend apparently common to a wide range of zirconium alloys (56). At the very start of the corrosion process, f_H^i increases markedly. Then at between 40% and 70% of the oxide transition thickness, f_H^i reaches a plateau. Finally, at approximately 70% of the oxide transition thickness, f_H^i starts to steadily increase again up to transition and appears to decrease just before the transition point (see **Figure 16*c***). Basically, f_H^i has an inverse relationship with the corrosion rate, with the differences between alloys due to different hydrogen pickup fractions.

Moreover, there is a correlation between f_H^t and oxidation kinetics for different alloys (56), suggesting a common oxidation and hydrogen pickup mechanism. These results, supported by previous studies (108–110), are plotted in **Figure 17**. An inverse relationship between the oxidation kinetics and f_H^t is clearly observed: the lower the n, the higher the f_H^t and vice versa. Nb-containing alloys also apparently have more parabolic kinetics and lower f_H^t relative to Zircaloy-type alloys. This correlation between oxidation kinetics and hydrogen pickup suggests a common corrosion mechanism such that any description of the hydrogen pickup should fit into a general corrosion mechanism. It seems indeed natural to consider that proton diffusion is one part of the cathodic reaction (the other one being electron transport) so that the corrosion rate to some extent depends on the resistances of these respective processes. This aspect has often been neglected in the literature; proposed mechanisms based on oxide microstructure evolution (53, 106), stress accumulation (111), cracks, and pore evolution (50, 112) often focus independently on the oxidation or the hydrogen pickup mechanism.

6. MODELING CORROSION AND HYDROGEN PICKUP

6.1. Coupled Current Charge Compensation Model

Under the assumption that oxygen diffusion is rate limiting, some explanations of zirconium alloys' subparabolic kinetics based on oxygen atom diffusion under a concentration gradient (Fick's law) have been proposed in the literature. The subparabolic kinetics would be explained as arising from differing oxygen anion transport for differing mechanisms, such as the accumulation of stress (111, 112), the creation of cracks in the oxide (50), and the change in grain size as the oxide grows (53). Although it is known that zirconium oxide can grow under anodic polarization (113) and that photo-electrochemical radiation changes the corrosion properties (such as the measured electric potential) in situ (114), none of the above mechanisms deal with the predominant charge state of the oxygen vacancy (or oxygen anion) or with the resulting electric field across the oxide. This electric field is inherent to the corrosion process and cannot be neglected.

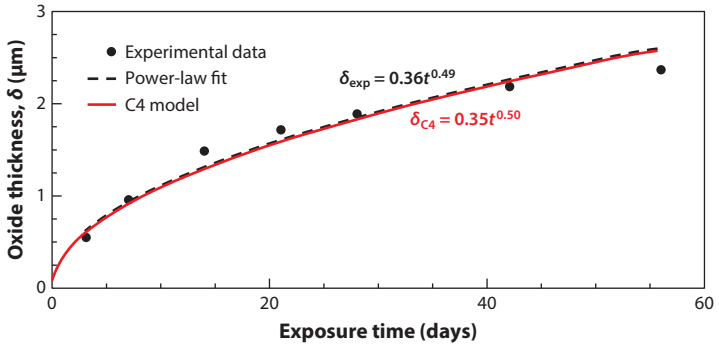

Figure 18

Oxidation kinetics of a Zr–0.4% Nb alloy along with the power-law fit (*dashed black line*) and the coupled current charge compensation (C4) oxidation model results (*red line*).

A general oxidation mechanism of zirconium alloys should be based on the existence of an electric field and on the condition that the necessary coupled electron current (cathodic current) be equal in magnitude but opposite in charge to the anionic current so that the net current across the oxide is zero. The oxygen anion flux must be balanced by the electron flux in the opposite direction. Thus, it seems reasonable to consider that to grow micrometer-scale oxides during thermal oxidation, the effect of electron transport and electric field has to be considered (11, 115, 116). Since Wagner's theory of local chemical potential equilibrium of charged species (51), various metal oxidation theories modeling the electric field have been applied to zirconium alloys. However, such models have not been able to reproduce oxidation kinetic differences between alloys and/or the associated hydrogen pickup (117, 118). Indeed, most of these models assume that cathodic current does not impact anionic current (and thus oxide growth), even though the two are coupled. In that sense, space charge theory can more readily explain subparabolic kinetics (119). Very few studies have attempted to apply this theory to zirconium oxidation (120, 121), even though their results are convincing.

To understand the oxidation and hydrogen pickup observations in zirconium alloys, a space charge oxidation model termed the coupled current charge compensation (C4) model has been developed (122). The model is based on Fromhold's (119) theory of a zero net current through the oxide (anionic current and cathodic current compensate each other) so that the concentrations of the two diffusing species, oxygen vacancies and electrons, do not necessarily compensate locally, creating space charge in the oxide.

6.2. Effect of Space Charge on the Oxidation Kinetics

Assuming that concentrations of defects at the oxide/metal and oxide/water interfaces and the relative migration energies do not significantly depend on the investigated alloys, the C4 model shows that the extent to which the parabolic oxidation is modified is proportional to the amount of space charge in the oxide (119). If this assertion were applied to the experimental observations (see **Figure 17**), ZrNb alloys would accumulate less space charge in their oxides during corrosion than would Zircaloys.

By using physically significant parameters, the parabolic oxidation kinetics of a Zr–0.4% Nb alloy can be reproduced if one assumes that space charges in the oxide are fully compensated so that there is no effect of space charges on the kinetics (122). **Figure 18** shows plots of the

experimental data and the associated power-law fit as well as the results of the model using the parameters displayed in **Table 2**.

This study concludes that, to account for parabolic kinetics, space charges need to be compensated for by acceptor substitutional aliovalent ions embedded in the oxide (122). The amount of oxidized Nb as a function of oxide depth was measured by μ-XANES in a Zr–0.4% Nb oxide, and there is enough oxidized Nb in solid solution to fully compensate for the space charges (originally due to local anion and electron concentration differences). In that case, the Nb oxidation state (for NbO and Nb_2O_3 oxides) is expected to be lower than 4+, which XANES experiments have confirmed (81, 83, 84). In contrast, the Fe and Cr solubility limit in the oxide is too low to provide charge compensation, which results in subparabolic oxidation kinetics in ZrFeCr alloys (including Zircaloys). The oxidation state and effect of Sn, as well as the effect of precipitates, are more difficult to model because of a general lack of experimental data and are still under investigation.

6.3. Relationship Between Oxidation Kinetics and Hydrogen Pickup Fraction

A direct observation of the C4 model is that, as the positive space charge in the oxide increases, the oxide electronic conductivity $\sigma_{e^-}^{ox}$ decreases. Indeed, as a consequence of the dependence of the electric field generated by space charge (from Poisson's equation) on oxide thickness, electron transport is altered as the oxide grows, and the oxidation kinetics deviates from parabolic to subparabolic. In situ electrochemical impedance spectroscopy (EIS) experiments were performed to measure $\sigma_{e^-}^{ox}$ on ZrNb and Zircaloy-4 alloys with similar pretransition oxide thicknesses (122, 123). The results show that $\sigma_{e^-}^{ox}$ of ZrNb alloy is one order of magnitude higher than $\sigma_{e^-}^{ox}$ of Zircaloy-4, with a range of values agreeing with the results of the C4 model.

From our understanding of the corrosion process, electron transport and proton transport are parallel processes, and the addition of their currents results in the total cathodic current. Because $\sigma_{e^-}^{ox}$ is higher for ZrNb alloys than for Zircaloy-4, for a given corrosion potential and cathodic current, the proton current must be higher for Zircaloy-4 than for ZrNb alloys. Consequently, $f_H^t(\text{Zr4}) > f_H^t(\text{ZrNb})$, a trend confirmed by experimental observations (56, 109, 124). Thus, $\sigma_{e^-}^{ox}$ has an inverse relationship with hydrogen pickup absorption; the electric potential across the oxide is the driving force for hydrogen pickup. This observation is more qualitative than quantitative, but it does bring a clear understanding to why hydrogen pickup fraction is lower for ZrNb alloys than for Zircaloy-4. The investigation of the dependence of hydrogen absorption on the applied potential would certainly give a quantitative relationship between these two physical entities.

Table 2 Values of the various parameters chosen to model Zr–0.4% Nb oxidation kinetics

Parameters	Value
Electron untrapping energy ($E_m^{e^-}$)	1 eV
Vacancy migration energy ($E_m^{V_O^{\cdot\cdot}}$)	1.58 eV
Migration distance (a)	5 Å
Temperature (T)	633 K
Concentration of vacancies at the oxide/metal interface [$C_{V_O^{\cdot\cdot}}(0)$]	4.2×10^{20} vacancies/cm^3
Concentration of electrons at the oxide/metal interface [$C_{e^-}(0)$]	8.4×10^{20} electrons/cm^3
Concentration of vacancies at the oxide/water interface [$C_{V_O^{\cdot\cdot}}(\delta)$]	10^{17} vacancies/cm^3
Concentration of electrons at the oxide/water interface [$C_{e^-}(\delta)$]	10^{17} electrons/cm^3

6.4. Evolution of Hydrogen Pickup Fraction as a Function of Exposure Time

One of the main observations related to hydrogen pickup fraction is that it changes significantly with exposure time, as mentioned above. On the basis of the hypotheses developed from the C4 model, these variations could be explained by a change in the hydrogen pickup driving force as a function of exposure time. In this context, the oxide electronic conductivity has been measured in situ by EIS as a function of exposure time on Zircaloy-4; the technique is extensively detailed in References 123, 125, and 126.

Although it is a material property independent of oxide thickness, the Zircaloy-4 oxide conductivity $\sigma_{e^-}^{ox}$ is not constant as a function of exposure time so that the electron transport is altered as the oxide grows and the hydrogen pickup driving force varies. Preliminary results show that $\sigma_{e^-}^{ox}$ is inversely proportional to f_H^i, confirming that the electric potential across the oxide is the main driving force for hydrogen pickup. These preliminary results indicate that oxide electronic conductivity has a key role in the hydrogen pickup mechanism. The reasons for $\sigma_{e^-}^{ox}$ variations are under investigation.

Space charges in the oxide should not significantly vary after the oxide thickness reaches 1 μm. The effect of delayed oxidation of metallic precipitates embedded in the oxide or the accumulation of compressive stresses in the oxide would more likely alter electron transport and is under investigation. In any case, electron transport and proton absorption in the oxide are competitive processes that are part of the corrosion cathodic current. Any variations of $\sigma_{e^-}^{ox}$ would be directly counterbalanced by a similar but opposite variation of proton migration through the oxide.

7. CONCLUSIONS

Waterside corrosion of zirconium alloy nuclear fuel cladding and the associated hydrogen pickup continue to be potential limiting factors for the operation of nuclear fuel to high burnup and more extreme conditions. Extensive research and development have created modern alloys that show considerable improvement in corrosion performance relative to traditional alloys. Mechanistic understanding of the corrosion process continues to be developed, although significant progress has been made in the understanding of the connection between alloy composition and microstructure, oxide structure, and corrosion behavior, as reviewed in this article. Nevertheless, considerable work remains to develop further mechanistic understanding and specifically the role of precipitates in the corrosion process, the exact nature of the stress accumulation process, and the mechanism of corrosion enhancement in reactor. The use of advanced characterization techniques, in situ experiments, and in-pile tests offers the prospect of greater mechanistic understanding of this complex process.

SUMMARY POINTS

1. Corrosion performance depends strongly on the alloy. Zirconium alloys are unique in that very small changes in alloy composition or microstructure can cause significant differences, both in corrosion rate (pretransition kinetics) and in oxide stability (transition or breakaway kinetics). The alloys show different but reproducible pretransition kinetics and transition thicknesses when tested in 360° water. The behavior of these alloys in autoclave tests generally correlates with their greater or lesser corrosion in reactor and provides guidance in the development of new alloys.

2. The mobile species appear to be oxygen atoms (diffusing by a vacancy mechanism), electrons, and hydrogen atoms. The relative balance between electrons and hydrogen transport determines hydrogen pickup.
3. The pretransition kinetics is related to the hydrogen pickup fraction of each alloy such that the closer the corrosion kinetics is to parabolic, the lower is the hydrogen pickup. The hydrogen pickup fraction varies during corrosion in a reproducible fashion and depends on the alloys. The oxide transition occurs at reproducible thicknesses for a given alloy in a given environment.
4. Oxide breakup—whether recoverable, such as during oxide transition, or unstable, such as during breakaway corrosion—is related to both stress accumulation and the development of porosity in the oxide layer. A mechanism for oxide growth and breakup that explains these results has been proposed on the basis of the results of a combination of various state-of-the-art experiments of the oxide structure.
5. The C4 model of both corrosion kinetics and hydrogen pickup provides a framework to rationalize both the subparabolic kinetics and the hydrogen pickup as a function of oxide conductivity. Hydrogen pickup increases when electron transport becomes more difficult, requiring hydrogen ingress to close the reaction.

DISCLOSURE STATEMENT

The authors are not aware of any affiliations, memberships, funding, or financial holdings that might be perceived as affecting the objectivity of this review.

LITERATURE CITED

1. IAEA. 2010. *Review of fuel failures in water cooled reactors*. Nucl. Energy Ser. NF-T-2.1, IAEA
2. Lustman B. 1979. Zirconium technology—twenty years of evolution. In *4th International Symposium on Zirconium in the Nuclear Industry*, ASTM STP 681, pp. 5–18. West Conshohocken, PA: ASTM Int.
3. Rickover HG, Geiger LD, Lustman B. 1975. *History of the development of zirconium alloys for use in nuclear reactors*. Rep., Energy Res. Dev. Admin./Div. Naval React., Washington, DC
4. Hillner E. 1977. Corrosion of zirconium base alloys—an overview. In *3rd International Symposium on Zirconium in the Nuclear Industry*, ASTM STP 633, pp. 211–35. West Conshohocken, PA: ASTM Int.
5. Kass S. 1964. The development of the zircaloys. In *Symposium on Corrosion of Zirconium Alloys* (*1963*), STP 368, pp. 3–27. New York: ANS
6. Sabol GP. 2005. ZIRLO: an alloy development success. In *14th International Symposium on Zirconium in the Nuclear Industry*, ASTM STP 1467, pp. 3–24. West Conshohocken, PA: ASTM Int.
7. Sabol GP, Kilp GR, Balfour MG, Roberts E. 1989. Development of a cladding alloy for high burnup. In *8th International Symposium on Zirconium in the Nuclear Industry*, ASTM STP 1023. West Conshohocken, PA: ASTM Int.
8. Mardon JP, Charquet D, Senevat J. 2000. Influence of composition and fabrication process on out-of-pile and in-pile properties of M5 alloy. In *12th International Symposium on Zirconium in the Nuclear Industry*, ASTM STP 1354, pp. 505–24. West Conshohocken, PA: ASTM Int.
9. Armijo JS, Coffin L, Rosenbaun H. 1995. Development of zirconium–barrier fuel cladding. In *11th International Symposium on Zirconium in the Nuclear Industry*, ASTM STP 1245, pp. 3–18. West Conshohocken, PA: ASTM Int.
10. Cox B. 2003. Mechanisms of zirconium alloy corrosion in nuclear reactors. *J. Corros. Sci. Eng.* 6:14
11. Cox B. 2005. Some thoughts on the mechanisms of in-reactor corrosion of zirconium alloys. *J. Nucl. Mater.* 336:331–68

12. IAEA. 1993. *Corrosion of zirconium alloys in nuclear power plants*. IAEA-TECDOC-684, IAEA
13. IAEA. 1998. Waterside corrosion of zirconium alloys in nuclear power plants. IAEA-TECDOC-996, IAEA
14. Allen TR, Konings RJM,Motta AT. 2012. Corrosion of zirconium alloys. In *Comprehensive Nuclear Materials*, Vol. 5, ed. RJM Konings, pp. 49–68. Oxford, UK: Elsevier
15. Motta AT. 2011. Waterside corrosion in zirconium alloys. *J. Met.* 63:59–63
16. Sabol GP, Comstock RJ, Weiner RA, Larouere P, Stanutz RN. 1994. In-reactor corrosion performance of ZIRLO and Zircaloy-4. In *10th International Symposium on Zirconium in the Nuclear Industry*, ASTM STP 1245, pp. 724–44. West Conshohocken, PA: ASTM Int.
17. Leech WJ, Yueh K. 2001. The fuel duty index, a method to assess fuel performance. In *Proceedings of International Conference on Light Water Reactor Fuel Performance* (*Top Fuel 2001*), pp. 2–16. La Grange Park, IL: ANS
18. Mardon JP, Charquet D, Senevat J. 1994. Development of new zirconium alloys for PWR fuel rod cladding. In *Proceedings of International Conference on Light Water Reactor Fuel Performance* (*Top Fuel 1994*), pp. 643–49. La Grange Park, IL: ANS
19. Mardon JP, Garner G, Beslu P, Charquet D, Senevat J. 1997. Update on the development of advanced zirconium alloys for PWR fuel rod claddings. In *Proceedings of International Conference on Light Water Reactor Fuel Performance* (*Top Fuel 1997*), pp. 405–12. La Grange Park, IL: ANS
20. Pan G, Garde AM, Atwood AR, Kallstrom R, Jadernas D. 2013. High burnup Optimized ZIRLO cladding performance. In *Proceedings of International Conference on Light Water Reactor Fuel Performance* (*Top Fuel 2013*), pp. 1–8. La Grange Park, IL: ANS
21. Mitchell D, Garde A, Davis D. 2010. Optimized ZIRLO fuel performance in Westinghouse PWRs. In *Proceedings of International Conference on Light Water Reactor Fuel Performance* (*Top Fuel 2010*), pp. 107–14. La Grange Park, IL: ANS
22. Romero J, Hallstadius L, Owaki M, Pan G, Kataoka K et al. 2014. Evolution of Westinghouse fuel cladding. In *Proceedings of International Conference on Light Water Reactor Fuel Performance* (*Top Fuel 2014*), Pap. 100019. La Grange Park, IL: ANS
23. Yoshino A, Ono S, Kido T, Onooka H. 2014. Irradiation behavior of J-Alloy™ at high burnup. *Proceedings of International Conference on Light Water Reactor Fuel Performance* (*Top Fuel 2014*), Pap. 100153. La Grange Park, IL: ANS
24. Pan G, Long CJ, Garde AM, Atwood AR, Foster JP et al. 2010. Advanced material for PWR application: AXIOM cladding. In *Proceedings of International Conference on Light Water Reactor Fuel Performance* (*Top Fuel 2010*), Pap. 074. La Grange Park, IL: ANS
25. Mardon JP, Garner GL, Hoffmann PB. 2010. M5® a breakthrough in Zr alloy. In *Proceedings of International Conference on Light Water Reactor Fuel Performance* (*Top Fuel 2010*), Pap. 069. La Grange Park, IL: ANS
26. Motta AT, Yilmazbayhan A, Comstock RJ, Partezana J, Sabol GP, et al. 2005. Microstructure and growth mechanism of oxide layers formed on Zr alloys studied with micro-beam synchrotron radiation. In *14th International Symposium on Zirconium in the Nuclear Industry*, ASTM STP 1467, pp. 205–32. West Conshohocken, PA: ASTM Int.
27. Arima T, Moriyama K, Gaja N, Furuya H, Idemitsu K, Inagaki Y. 1998. Oxidation kinetics of Zircaloy-2 between 450°C and 600°C in oxidizing atmosphere. *J. Nucl. Mater.* 257:67–77
28. Fuketa T, Nagase F, Ishijima K, Fujishiro T. 1996. NSRRRIA experiments with high burnup PWR fuels. *Nucl. Saf.* 37:328–42
29. Couet A, Motta AT, Comstock RJ. 2013. Effect of alloying elements on hydrogen pick-up in zirconium alloys. In *17th International Symposium on Zirconium in the Nuclear Industry*, ASTM STP 1543, pp 479–514. West Conshohocken, PA: ASTM Int.
30. Ma X, Toffolon-Masclet C, Guilbert T, Hamon D, Brachet JC. 2008. Oxidation kinetics and oxygen diffusion in low-tin Zircaloy-4 up to 1523 K. *J. Nucl. Mater.* 377:359–69
31. Fromhold AT. 1972. Parabolic oxidation of metals in homogeneous electric fields. *J. Phys. Chem. Solids* 33:95–120
32. Fromhold AT. 1978. Distribution of charge and potential through oxide films. *J. Electrochem. Soc.* 125:C118–18

33. Fromhold AT. 1979. Easy insight into space-charge effects on steady-state transport in oxide films. *Oxid. Met.* 13:475–79
34. Cox B, Pemsler JP. 1968. Diffusion of oxygen in growing zirconia films. *J. Nucl. Mater.* 28:73–78
35. Cox B. 1968. Effect of irradiation on the oxidation of zirconium alloys in high temperature aqueous environments: a review. *J. Nucl. Mater.* 28:1–47
36. Ramasubramanian N. 1975. Localised electron transport in corroding zirconium alloys. *J. Nucl. Mater.* 55:34–54
37. Motta AT, Chen LQ. 2012. Hydride formation in zirconium alloys. *J. Met.* 64:1403–8
38. Motta AT, Gomes Da Silva MJ, Yilmazbayhan A, Comstock RJ, Cai Z, Lai B. 2009. Microstructural characterization of oxides formed on model Zr alloys using synchrotron radiation. In *15th International Symposium on Zirconium in the Nuclear Industry*, ASTM STP 1505, pp. 486–506. West Conshohocken, PA: ASTM Int.
39. Inagaki M, Kanno M, Maki H. 1991. Effect of alloying elements in zircaloy on photoelectrochemical characteristics of zirconium-oxide films. In *9th International Symposium on Zirconium in the Nuclear Industry*, ASTM STP 1132, pp. 437–60. West Conshohocken, PA: ASTM Int.
40. Kofstad P, Ruzicka DJ. 1963. On the defect structure of ZrO_2 and HfO_2. *J. Electrochem. Soc.* 110:181–84
41. Grandjean A, Serruys Y. 1999. Metal and oxygen mobilities during Zircaloy-4 oxidation at high temperature. *J. Nucl. Mater.* 273:111–15
42. Cox B, Pemsler JP. 1968. Diffusion of oxygen in growing zirconia films. *J. Nucl. Mater.* 28:73–78
43. Yilmazbayhan A, Motta AT, Comstock RJ, Sabol GP, Lai B, Cai Z. 2004. Structure of zirconium alloy oxides formed in pure water studied with synchrotron radiation and optical microscopy: relation to corrosion rate. *J. Nucl. Mater.* 324:6–22
44. Douglass DL. 1971. *The Metallurgy of Zirconium*. Vienna: IAEA
45. Cox B. 1987. Pore structure in oxide films on irradiated and unirradiated zirconium alloys. *J. Nucl. Mater.* 148:332–43
46. Maroto AJG, Bordoni R, Villegas M, Olmedo AM, Blesa MA, et al. 1996. Growth and characterization of oxide layers on zirconium alloys. *J. Nucl. Mater.* 229:79–92
47. Cox B. 1969. Processes occurring during the breakdown of oxide films on zirconium alloys. *J. Nucl. Mater.* 29:50–66
48. Lemaignan C, Motta AT. 1994. Zirconium alloys in nuclear applications. In *Materials Science and Technology*, Vol. 10, ed. BRT Frost, pp. 1–51. New York: Wiley
49. Cox B. 1969. Rate controlling processes during the pre-transition oxidation of zirconium alloys. *J. Nucl. Mater.* 31:48–66
50. Tupin M, Pijolat M, Valdivieso F, Soustelle M, Frichet A, Barberis P. 2003. Differences in reactivity of oxide growth during the oxidation of Zircaloy-4 in water vapour before and after the kinetic transition. *J. Nucl. Mater.* 317:130–44
51. Hauffe K. 1965. *Oxidation of Metals*. Oxford, UK: Plenum
52. Fromhold AT. 1975. *Theory of Metal Oxidation*. Amsterdam: North-Holland
53. Sabol GP, Dalgaard SB. 1975. The origin of the cubic rate law in zirconium alloy oxidation. *J. Electrochem. Soc.* 122:316–17
54. Porte HA, Schnizlein JG, Vogel RC, Fischer DF. 1960. Oxidation of zirconium and zirconium alloys. *J. Electrochem. Soc.* 107:506–15
55. Yilmazbayhan A, Motta AT, Comstock RJ, Sabol GP, Lai B, Cai Z. 2004. Structure of zirconium alloy oxides formed in pure water studied with synchrotron radiation and optical microscopy: relation to corrosion rate. *J. Nucl. Mater.* 324:6–22
56. Couet A, Motta AT, Comstock RJ. 2014. Hydrogen pickup measurements in zirconium alloys: relation to oxidation kinetics. *J. Nucl. Mater.* 451:1–13
57. Wagner C, Schottky W. 1930. Theory of controlled mixed phases. *Z. Phys. Chem.* 11:163–210
58. Couet A, Motta AT, Comstock RJ, Paul RL. 2012. Cold neutron prompt gamma activation analysis, a non-destructive technique for hydrogen level assessment in zirconium alloys. *J. Nucl. Mater.* 425:211–17
59. Cox B, Roy C. 1965. *The use of tritium as a tracer in studies of hydrogen uptake by zirconium alloys*. AECL 2519, Chalk River Nucl. Lab., At. Energy Can.

60. Kass S, Kirk WW. 1962. Corrosion and hydrogen absorption properties of nickel-free Zircaloy-2 and Zircaloy-4. *ASM Trans. Q.* 55:77–100
61. Garde AM, Slagle H, Mitchell D. 2009. Hydrogen pick-up fraction for ZIRLO cladding corrosion and resulting impact on the cladding integrity. In *Proceedings of International Conference on Light Water Reactor Fuel Performance* (*Top Fuel 2009*), Pap. 2136. La Grange Park, IL: ANS
62. Wanklyn JN, Silvester DR, Dalton J, Wilkins NJM. 1961. *The Corrosion of Zirconium and Its Alloys in High Temperature Steam. Part II: The Uptake of Hydrogen During Corrosion*. Harwell, UK: At. Energy Res. Establ.
63. Baur K, Garzarolli F, Ruhmann H, Sell H-J. 2000. Electrochemical examinations in 350°C water with respect to the mechanism of corrosion-hydrogen pickup. In *12th International Symposium on Zirconium in the Nuclear Industry*, ASTM STP 1354, pp. 836–52. West Conshohocken, PA: ASTM Int.
64. Ramasubramanian N, Billot P, Yagnik S. 2002. Hydrogen evolution and pickup during the corrosion of zirconium alloys: a critical evaluation of the solid state and porous oxide electrochemistry. In *13th International Symposium on Zirconium in the Nuclear Industry*, ASTM STP 1423, pp. 222–44. West Conshohocken, PA: ASTM Int.
65. Gabory BD, Motta AT. 2013. Structure of Zircaloy 4 oxides formed during autoclave corrosion. In *Light Water Reactor Fuel Performance Meeting* (*Top Fuel 2013*), Pap. 8584. La Grange Park, IL: ANS
66. Li H, Glavicic HM, Szpunar JA. 2004. A model of texture formation in ZrO_2 films. *Mater. Sci. Eng. A* 366:164–74
67. Pétigny N, Barberis P, Lemaignan C, Valot C, Lallemant M. 2000. In situ XRD analysis of the oxide layers formed by oxidation at 743 K on Zircaloy-4 and Zr-1NbO. *J. Nucl. Mater.* 280:318–30
68. Polatidis E, Frankel P, Wei J, Klaus M, Comstock RJ, et al. 2013. Residual stresses and tetragonal phase fraction characterisation of corrosion tested Zircaloy-4 using energy dispersive synchrotron X-ray diffraction. *J. Nucl. Mater.* 432:102–12
69. Cox B. 1968. A porosimeter for determining the sizes of flaws in zirconia or other insulating films "in-situ". *J. Nucl. Mater.* 27:1–11
70. Cox B, Yamaguchi Y. 1994. The development of porosity in thick zirconia films. *J. Nucl. Mater.* 210:303–17
71. Ni N, Lozano-Perez S, Jenkins ML, English C, Smith GDW, et al. 2010. Porosity in oxides on zirconium fuel cladding alloys, and its importance in controlling oxidation rates. *Scr. Mater.* 62:564–67
72. Ni N, Lozano-Perez S, Sykes J, Grovenor C. 2012. Multi-scale characterisation of oxide on zirconium alloys. *Mater. High Temp.* 29:166–70
73. Ni N, Hudson D, Wei J, Wang P, Lozano-Perez S, et al. 2012. How the crystallography and nanoscale chemistry of the metal-oxide interface develops during the aqueous oxidation of zirconium cladding alloys. *Acta Mater.* 60:7132–49
74. Yardley SS, Moore KL, Na N, Wei JF, Lyon S, et al. 2013. An investigation of the oxidation behaviour of zirconium alloys using isotopic tracers and high resolution SIMS. *J. Nucl. Mater.* 443:436–43
75. Bechade J-L, Brenner R, Goudeau P, Gailhanou M. 2003. Determination des contraintes internes dans une couche de zircone par diffraction des rayons X et par une approche micromecanique: influence de l'anisotropie thermoelastique. *Rev. Metall.* 2003:1151–56
76. Béchade J-L, Brenner R, Goudeau P, Gailhanou M. 2002. Influence of temperature on X-ray diffraction analysis of ZrO_2 oxide layers formed on zirconium based alloys using a synchrotron radiation. *Mater. Sci. Forum* 404–407:803–8
77. Goudeau P, Faurie D, Girault B, Renault PO, Le Bourhis E, et al. 2006. Strains, stresses and elastic properties in polycrystalline metallic thin films: in situ deformation combined with X-ray diffraction and simulation experiments. *Mater. Sci. Forum* 524–525:735–40
78. Pecheur D, Lefebvre F, Motta AT, Lemaignan C, Charquet D. 1994. Oxidation of intermetallic precipitates in Zircaloy-4: impact of irradiation. In *10th International Symposium on Zirconium in the Nuclear Industry*, ASTM STP 1245, pp. 687–70. West Conshohocken, PA: ASTM Int.
79. Pecheur D, Lefebvre F, Motta AT, Lemaignan C, Wadier J-F. 1992. Precipitate evolution in the Zircaloy-4 oxide layer. *J. Nucl. Mater.* 189:2318–32
80. Yilmazbayhan A, Breval E, Motta A, Comstock R. 2006. Transmission electron microscopy examination of oxide layers formed in Zr alloys. *J. Nucl. Mater.* 349:265–81

81. Froideval A, Abolhassani S, Gavillet D, Grolimund D, Borca C, et al. 2009. Microprobe analysis of neutron irradiated and autoclaved zirconium niobium claddings using synchrotron-based hard X-ray imaging and spectroscopy. *J. Nucl. Mater.* 385:346–50
82. Sakamoto K, Une K, Aomi M. 2010. Chemical state of alloying elements in oxide layer of Zr-based alloys. In *Light Water Reactor Fuel Performance Meeting* (*Top Fuel 2010*), Pap. 13101. La Grange Park, IL: ANS
83. Sakamoto K, Une K, Aomi M, Hashizume K. 2012. Depth profile of chemical states of alloying elements in oxide layer of Zr-based alloys. *Prog. Nucl. Energy* 57:101–5
84. Couet A, Motta AT, de Gabory B, Cai Z. 2014. Microbeam X-ray absorption near-edge spectroscopy study of the oxidation of Fe and Nb in zirconium alloy oxide layers. *J. Nucl. Mater.* 452:614–27
85. Garvie RC, Nicholson PS. 1972. Structure and thermomechanical properties of partially stabilized zirconia in CaO-ZrO_2 system. *J. Am. Ceram. Soc.* 55:152–57
86. Polatidis E, Frankel P, Wei J, Klaus M, Comstock RJ, et al. 2013. Residual stresses and tetragonal phase fraction characterisation of corrosion tested Zircaloy-4 using energy dispersive synchrotron X-ray diffraction. *J. Nucl. Mater.* 432:102–12
87. Deleted in proof
88. Takeda K, Anada H. 2000. Mechanism of corrosion degradation in Sn. In *12th International Symposium on Zirconium in the Nuclear Industry*, ASTM STP 1354, pp. 592–608. West Conshohocken, PA: ASTM Int.
89. Abriata JP, Garces J, Versaci R. 1986. The Zr-O (zirconium-oxygen) system. *Bull. Alloy Phase Diagr.* 7:116–24
90. Warr BD, Elmoselhi M, Newcomb SB, McIntyre NS, Brennenstuhl AM, Lichtenberger PC. 1991. Oxide characteristics and their relationship to hydrogen uptake in zirconium alloys. In *9th International Symposium on Zirconium in the Nuclear Industry*, ASTM STP 1132, pp. 740–57. West Conshohocken, PA: ASTM Int.
91. Iltis X, Lefebvre F, Lemaignan C. 1995. Microstructural study of oxide layers formed on Zircaloy-4 in autoclave and in reactor. Part II. Impact of the chemical evolution of intermetallic precipitates on their zirconia environment. *J. Nucl. Mater.* 224:121–30
92. Hutchinson B, Lehtinen B, Limbach M, Dahlback M. 2009. A study of the structure and chemistry in Zircaloy-2 and the resulting oxide after high temperature corrosion. In *15th International Symposium on Zirconium in the Nuclear Industry*, ASTM STP 1505, pp. 269–84. West Conshohocken, PA: ASTM Int.
93. Hudson D, Ni N, Lozano-Perez S, Saxey D, English C, et al. 2009. The atomic scale structure and chemistry of the Zircaloy-4 metal-oxide interface. In *14th International Conference on Environmental Degradation of Materials in Nuclear Power Systems Water Reactors*, pp. 1407–18. Warrendale, PA: TMS
94. Ni N, Lozano-Perez S, Sykes J, Grovenor C. 2011. Quantitative EELS analysis of zirconium alloy metaloxide interfaces. *Ultramicroscopy* 111:123–30
95. Dong Y, Motta AT, Marquis EA. 2013. Atom probe tomography study of alloying element distributions in Zr alloys and their oxides. *J. Nucl. Mater.* 442:270–81
96. Gabory BD, Motta AT, Wang K. 2015. Transmission electron microscopy characterization of Zircaloy-4 and ZIRLO^{TM} oxide layers. *J. Nucl. Mater.* 456:272–80
97. Peng Q, Gartner E, Busby JT, Motta AT, Was GS. 2007. Corrosion behavior of model zirconium alloys in deaerated supercritical water at 500°C. *Corrosion* 63:577–90
98. Cox B, Wong YM. 1999. A hydrogen uptake micro-mechanism for Zr alloys. *J. Nucl. Mater.* 270:134–46
99. Veshchunov MS, Berdyshev AV. 1998. Modelling of hydrogen absorption by zirconium alloys during high temperature oxidation in steam. *J. Nucl. Mater.* 255(2–3):250–62
100. Hatano Y, Sugisaki M, Kitano K, Hayashi M. 2000. Role of intermetallic precipitates in hydrogen transport through oxide films on Zircaloy. In *12th International Symposium on Zirconium in the Nuclear Industry*, ASTM STP 1354, pp. 901–17. West Conshohocken, PA: ASTM Int.
101. Draley JE, Ruther WE. 1957. Some unusual effects of hydrogen in corrosion reactions. *J. Electrochem. Soc.* 104:329–33
102. Berry WE, Vaughan DA, White EL. 1961. Hydrogen pickup during aqueous corrosion of zirconium alloys. *Corrosion* 17:109–17

103. Kass S. 1960. Hydrogen pickup in various zirconium alloys during corrosion exposure in high-temperature water and steam. *J. Electrochem. Soc.* 107:594–97
104. Hillner E. 1964. *Hydrogen absorption in Zircaloy during aqueous corrosion: effect of environment*. Res. Dev. Rep. WAPD-TM-411, US At. Energy Comm.
105. Adamson R, Garzarolli F, Cox B, Strasser A, Rudling P. 2007. *Corrosion mechanisms in zirconium alloys*. Rep., ANT Int.
106. Harada M, Wakamatsu R. 2008. The effect of hydrogen on the transition behavior of the corrosion rate of zirconium alloys. In *15th International Symposium on Zirconium in the Nuclear Industry*, ASTM STP 1505, pp. 384–400. West Conshohocken, PA: ASTM Int.
107. Une K, Sakamoto K, Aomi M, Matsunaga J, Etoh Y, et al. 2011. Hydrogen absorption mechanism of zirconium alloys based on characterization of oxide layer. In *16th International Symposium on Zirconium in the Nuclear Industry*, ASTM STP 1529, pp. 401–32. West Conshohocken, PA: ASTM Int.
108. Broy Y, Garzarolli F, Seibold A, Van Swam LF. 2000. Influence of transition elements Fe, Cr, and V on long-time corrosion in PWRs. In *12th International Symposium on Zirconium in the Nuclear Industry*, ASTM STP 1354, pp. 609–22. West Conshohocken, PA: ASTM Int.
109. Kiselev AA. 1963. *Research on the corrosion of zirconium alloys in water and steam at high temperature and pressure*. Rep. AECL-1724, At. Energy Can.
110. Murai T, Isobe K, Takizawa Y, Mae Y. 2000. Fundamental study on the corrosion mechanism of Zr-0.2Fe, Zr-0.2Cr and Zr-0.1Fe-0.2Cr alloys. In *12th International Symposium on Zirconium in the Nuclear Industry*, ASTM STP 1354, pp. 623–40. West Conshohocken, PA: ASTM Int.
111. Evans HE, Norfolk DJ, Swan T. 1978. Perturbation of parabolic kinetics resulting from the accumulation of stress in protective oxide layers. *J. Electrochem. Soc.* 125:1180–85
112. Dollins CC, Jursich M. 1983. A model for the oxidation of zirconium-based alloys. *J. Nucl. Mater.* 113:19–24
113. Ai J, Chen Y, Urquidi-Macdonald M, Macdonald DD. 2008. Electrochemical impedance spectroscopic study of passive zirconium. *J. Nucl. Mater.* 379:162–68
114. Kim Y-J, Rebak R, Lin Y-P, Lutz D, Crawford DC, et al. 2011. Photoelectrochemical investigation of radiation-enhanced shadow corrosion phenomenon. In *16th International Symposium on Zirconium in the Nuclear Industry*, ASTM STP 1529, pp. 91–116. West Conshohocken, PA: ASTM Int.
115. Tupin M, Bataillon C, Gozlan J-P, Bossis P. 2007. High temperature corrosion of Zircaloy-4. In *Electrochemistry in Light Water Reactors: Reference Electrodes, Measurement, Corrosion and Tribocorrosion Issues*, ed. RW Bosch, D Féron, JP Celis, pp. 134–55. Cambridge, UK: Eur. Fed. Corros.
116. Pauporte T, Finne J. 2006. Impedance spectroscopy study of anodic growth of thick zirconium oxide films in H_2SO_4, Na_2SO_4 and NaOH solutions. *J. Appl. Electrochem.* 36:33–41
117. Chen Y, Urquidi-Macdonald M, Macdonald DD. 2006. The electrochemistry of zirconium in aqueous solutions at elevated temperatures and pressures. *J. Nucl. Mater.* 348:133–47
118. Bojinov M, Karastoyanov V, Kinnunen P, Saario T. 2010. Influence of water chemistry on the corrosion mechanism of a zirconium-niobium alloy in simulated light water reactor coolant conditions. *Corros. Sci.* 52:54–67
119. Fromhold AT. 1980. *Theory of Metal Oxidation: Space Charge*. Amsterdam: North-Holland
120. Eloff GA, Greyling CJ, Viljoen PE. 1993. The role of space charge in the oxidation of Zircaloy-4 between 350 and 450°C in air. *J. Nucl. Mater.* 199:285–88
121. Beie H-J, Mitwalsky A, Garzarolli F, Ruhmann H, Sell HJ. 1994. Examinations of the corrosion mechanism of zirconium alloys. In *10th International Symposium on Zirconium in the Nuclear Industry*, ASTM STP 1245, pp. 615–43. West Conshohocken, PA: ASTM Int.
122. Couet A, Motta AT, Ambard A. 2014. The coupled current charge compensation model for zirconium alloy fuel cladding oxidation. I. Parabolic oxidation of zirconium alloys. *Corros. Sci.* Submitted
123. Couet A, Motta AT, Ambard A. 2014. *Oxide electronic conductivity and hydrogen pickup fraction in Zr alloys*. Presented at Annual Meeting on Transactions of the American Nuclear Society and Embedded Topical Meeting: Nuclear Fuels and Structural Materials for the Next Generation Nuclear Reactors (NSFM 2014), Reno, Nev., June 15–19

124. Thomazet J, Dalmais A, Bossis P, Godlewski J, Blat M, Miquet A. 2005. *The corrosion of the alloy M5: an overview*. Presented at IAEA Technical Committee Meeting on Behavior of High Corrosion Zr-Based Alloys, Buenos Aires, Oct. 24–28
125. Schefold J, Lincot D, Ambard A, Kerrec O. 2003. The cyclic nature of corrosion of Zr and Zr-Sn in high-temperature water (633 K)—a long-term in situ impedance spectroscopic study. *J. Electrochem. Soc.* 150:B451–61
126. Couet A. 2014. *Hydrogen pickup mechanism of zirconium alloys*. PhD Thesis, Dep. Mech. Nucl. Eng., Penn State Univ.
127. Bossis P, Pêcheur D, Hanifi K, Thomazet J, Blat M. 2005. Comparison of the high burn-up corrosion on M5 and low tin Zircaloy-4. In *14th International Symposium on Zirconium in the Nuclear Industry*, ASTM STP 1467, pp. 494–525. West Conshohocken, PA: ASTM Int.

Annual Review of Biophysics
Volume 44, 2015

Contents

Index

Errata

An online log of corrections to *Annual Review of Biophysics* articles may be found at http://www.annualreviews.org/errata/biophys